DOI:
10.1016/j.devcel.2022.02.001

Document Version
Publisher's PDF, also known as Version of record

Article

Developmental Cell

Physical properties of the cytoplasm modulate the rates of microtubule polymerization and depolymerization

Graphical abstract

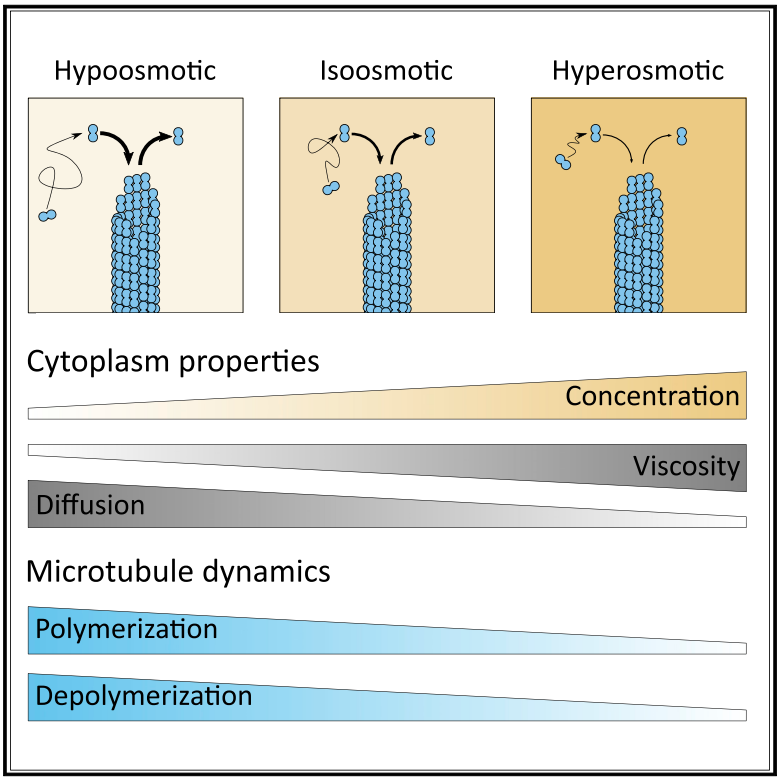

Authors

Arthur T. Molines, Joël Lemière, Morgan Gazzola, ..., Manuel Thery, Gary J. Brouhard, Fred Chang

Correspondence

a.t.molines@gmail.com (A.T.M.), fred.chang@ucsf.edu (F.C.)

In brief

How dynamic cellular processes operate in the complex environment of the cytoplasm remains poorly understood. Molines et al. show that the cytoplasm physically dampens microtubule assembly and disassembly through its viscous properties. These findings demonstrate the importance of cytoplasmic viscosity to biochemical reaction rates within the living cell.

Highlights

- Osmotic shifts modulate microtubule assembly and disassembly proportionally in cells
- Effects correlate with changes in cytoplasmic concentration, viscosity, and diffusion
- Effects are conserved across eukaryotes (yeast, plant, mammalian cells)
- Cytoplasmic dampening of microtubules is recapitulated by a viscous agent *in vitro*

Molines et al., 2022, Developmental Cell *57*, 466–479
February 28, 2022
https://doi.org/10.1016/j.devcel.2022.02.001

CellPress

CellPress
OPEN ACCESS

Developmental Cell

Article

Physical properties of the cytoplasm modulate the rates of microtubule polymerization and depolymerization

Arthur T. Molines,[1,9,*] Joël Lemière,[1] Morgan Gazzola,[2] Ida Emilie Steinmark,[3] Claire H. Edrington,[4] Chieh-Ting Hsu,[5] Paula Real-Calderon,[1] Klaus Suhling,[3] Gohta Goshima,[6,9] Liam J. Holt,[7,9] Manuel Thery,[2,8] Gary J. Brouhard,[4] and Fred Chang[1,9,10,*]

[1]Department of Cell and Tissue Biology, University of California, San Francisco, USA
[2]University of Grenoble-Alpes, CEA, CNRS, INRA, Interdisciplinary Research Institute of Grenoble, Laboratoire de Phyiologie Cellulaire & Vegétale, CytoMorpho Lab, 38054 Grenoble, France
[3]Department of Physics, King's College London, London, UK
[4]Department of Biology, McGill University, Montréal, Quebec, Canada
[5]Department of Physics, McGill University, Montréal, Quebec, Canada
[6]Sugashima Marine Biological Laboratory and Division of Biological Science, Graduate School of Science, Nagoya University, Toba City, Mie, Japan
[7]Institute for Systems Genetics, New York University Langone Health, New York, NY 10016, USA
[8]Université de Paris, INSERM, CEA, Institut de Recherche Saint Louis, U 976, CytoMorpho Lab, 75010 Paris, France
[9]Marine Biological Laboratory, Woods Hole, MA 02543, USA
[10]Lead contact
*Correspondence: a.t.molines@gmail.com (A.T.M.), fred.chang@ucsf.edu (F.C.)
https://doi.org/10.1016/j.devcel.2022.02.001

SUMMARY

The cytoplasm is a crowded, visco-elastic environment whose physical properties change according to physiological or developmental states. How the physical properties of the cytoplasm impact cellular functions *in vivo* remains poorly understood. Here, we probe the effects of cytoplasmic concentration on microtubules by applying osmotic shifts to fission yeast, moss, and mammalian cells. We show that the rates of both microtubule polymerization and depolymerization scale linearly and inversely with cytoplasmic concentration; an increase in cytoplasmic concentration decreases the rates of microtubule polymerization and depolymerization proportionally, whereas a decrease in cytoplasmic concentration leads to the opposite. Numerous lines of evidence indicate that these effects are due to changes in cytoplasmic viscosity rather than cellular stress responses or macromolecular crowding per se. We reconstituted these effects on microtubules *in vitro* by tuning viscosity. Our findings indicate that, even in normal conditions, the viscosity of the cytoplasm modulates the reactions that underlie microtubule dynamic behaviors.

INTRODUCTION

Cytoplasm is composed of 100–300 mg/mL of macromolecules (proteins, nucleic acids, lipids, etc.), which occupy 10%–40% of the total cellular volume (Milo and Phillips, 2015; Neurohr and Amon, 2020). These components range in size from small globular proteins to extended networks of organelles and cytoskeletal polymers. Ribosomes alone occupy ~20% of that volume (Delarue et al., 2018). Biophysical studies revealed that these constituents form a porous, visco-elastic material that allows diffusion of small molecules but impedes movement of larger particles (Luby-Phelps et al., 1986; Moeendarbary et al., 2013; Xiang et al., 2020), and molecular simulations show a high density of macromolecules jostling and colliding from diffusive motion (Mcguffee and Elcock, 2010; Yu et al., 2016).

In contrast to the density of inert materials, the density of the cytoplasm is regulated as part of cell physiology. Indeed, cytoplasmic density varies during the cell cycle, among different cell types, as a result of aging, as a response to nutritional stress, and as a response to disease (Neurohr and Amon, 2020). These density changes likely affect macromolecule concentrations and the physical properties of the cytoplasm, such as its degree of crowding and/or its viscosity, which in turn will impact a broad range of cellular processes, such as protein-protein associations, phase transitions, and enzymatic fluxes. It was also recently proposed that cells can tune the viscosity of their cytoplasm to regulate diffusion-dependent processes in response to temperature (Persson et al., 2020). Thus, it is critical to understand how cellular reactions are affected by the physical properties of the cytoplasm.

A prominent physical property of the cytoplasm is macromolecular crowding. There are several conceptual models used to describe the influence of macromolecular crowding on biochemical reactions. Minton and colleagues have argued that bulky macromolecules "exclude volume," a steric effect that increases the thermodynamic activity of other proteins (Minton, 2006; Shahid et al., 2017). Consistent with this idea, bulky macromolecules

often accelerate biochemical reactions *in vitro*. Additionally, because macromolecules are rarely inert, they interact with proteins via short-term, non-specific hydrophobic interactions that can affect the rates and equilibria of reactions (Mcguffee and Elcock, 2010). Theoretical models of macromolecular crowding can explain how crowding impedes diffusion, produces entropic forces that draw molecules together, promotes phase separation, and produces osmotic pressure within cells (Ellis, 2001; Mitchison, 2019; Shahid et al., 2017). But the models of macromolecular crowding do not always make the same predictions. For example, Mitchison used the concept of colloidal osmotic pressure to argue that cytoplasm is functionally dilute, such that a reaction like microtubule (MT) polymerization would be unaffected by steric effects *in vivo* (Mitchison, 2019). To distinguish between these concepts, what is needed are experiments that perturb the physical properties of the cytoplasm and measure the rates of cellular reactions *in vivo*.

The dynamic behavior of MTs represents an attractive system to probe the effects of the cytoplasm on defined biochemical reactions *in vivo*. First, the polymerization and depolymerization of single MTs are reactions that can be quantitatively measured in living cells and *in vitro* using microscopy. Second, the effects of macromolecular crowding on MTs *in vitro* are known: MTs grow significantly faster in the presence of bulky crowders but significantly slower in the presence of small viscous agents like glycerol (Wieczorek et al., 2013). These *in vitro* measurements can be compared with *in vivo* measurements when considering mechanisms. Third, the tubulin dimer, which is 100 kDa in mass and 8-nm in length, represents a size range typical for soluble proteins, while the MT end, which has a diameter of around 25 nm, is similar in size scale to that of large macromolecular complexes such as the ribosome. Finally, MT polymerization depends on tubulin concentration, while MT depolymerization does not (Fygenson et al., 1994; Walker et al., 1988). Thus, changes in tubulin concentration (e.g., because of changes in cytoplasmic concentration) should impact polymerization alone, which is a testable prediction of some models. Taken together, MTs are well suited to probe which properties of the cytoplasm have the strongest impact on cellular reactions and, more generally, to inform biophysical models describing the physical properties of the cytoplasm.

Fission yeast is an excellent model organism in which to study the physical regulation of MT dynamics *in vivo*. We can readily image the interphase MT bundles and measure the dynamic behavior of individual MTs with precision (Höög et al., 2007; Loiodice et al., 2019; Sawin and Tran, 2006). Various effects of osmotic shocks on fission yeast polarized cell growth and cytoskeleton have been described (Chowdhury et al., 1992; Haupt et al., 2018; Mutavchiev et al., 2016; Robertson and Hagan, 2008). Osmotic shifts create rapid changes in cellular volume, suggesting that such treatments can be used to tune cytoplasmic properties (Atilgan et al., 2015; Knapp et al., 2019).

Here, we study the effects of the physical properties of the cytoplasm on MT dynamics by using osmotic shifts to vary cytoplasmic concentration acutely. We show that hyperosmotic shifts, which increase cytoplasmic concentration, lead to dampening and "freezing" of MT polymerization and depolymerization. Conversely, hypoosmotic shifts, which decrease cytoplasmic concentration, lead to increased rates of MT polymerization and depolymerization. The observed proportionate changes to MT rates, which were independent of the osmotic stress response and key MT regulators, correlated with global changes in cytoplasmic physical properties and were recapitulated *in vitro* through modulation of viscosity. These findings demonstrate that the cytoplasm modulates MT dynamics through viscous effects even at normal concentrations of the cytoplasm.

RESULTS

Osmotic shifts modulate microtubule dynamics in cells

The density of cellular components can be experimentally manipulated by varying the osmotic environment using osmotic agents such as sorbitol (Knapp et al., 2019), which does not enter cells (Watari et al., 2004; Wood et al., 1968). An acute increase in external osmolarity leads to a corresponding increase in intracellular osmolarity (Beauzamy et al., 2014). We manipulated live fission yeast cells by adding sorbitol to the growth medium, which led to an acute decrease in cell volume in a dose-dependent, reversible manner (Figures 1A, S1, and S2) (Atilgan et al., 2015; Knapp et al., 2019). For instance, cell volume decreased by up to 50% with 1.5 M sorbitol added to rich media, without loss in cell viability (Figure S1). This volume decrease presumably occurred through water loss to cause a corresponding increase in macromolecule concentration (Beauzamy et al., 2014). Indeed, we confirmed the increase in macromolecule concentration by measuring fluorescence intensity of GFP-labeled tubulin and the ribosomal protein Rps802 in sorbitol-treated cells, as well as by refractive index measurements (Figure S1). Hence, hyperosmotic shocks can be used to acutely manipulate the intracellular concentration of macromolecules.

Having validated this approach to alter intracellular concentration, we applied it to cells expressing GFP-tubulin to monitor MT dynamics. Time-lapse imaging of untreated cells showed that interphase MTs were characteristically dynamic, polymerizing and depolymerizing, with little time in "pause" (Tran et al., 2001). In contrast, hyperosmotic shifts caused significant changes in the dynamic behaviors of interphase MTs, as noted previously (Robertson and Hagan, 2008; Tatebe et al., 2005). We found that in acute response to hyperosmotic shifts, the interphase MT cytoskeleton appeared to "freeze" (Figures 1B and 1C), especially at high sorbitol concentrations (e.g., 1.5 M) (Figures 1B–1D). In general, MTs were "paused" at various lengths and exhibited little or no polymerization or depolymerization. To determine whether the effects of the hyperosmotic shifts were reversible, we cycled the concentration of sorbitol from 0 to 1.5 M in 5-min intervals. Upon each hyperosmotic shift to 1.5 M sorbitol, most of the MTs "froze" within 30 s (Figures 1B and 1C; Video S1). Upon each shift back to sorbitol-free medium, all interphase MTs promptly went into catastrophe, shrank toward the middle of the cell, and then regrew, such that the normal interphase array was restored in a few minutes (<5 min) (Figures 1B and S2). The prompt catastrophes suggest that the GTP cap is hydrolyzed when MTs are in the "frozen" state. This cycle of MT "freezing" and resumption of dynamics could be induced repeatedly (Figures 1B and S2), demonstrating that the effects of hyperosmotic shifts were rapid and reversible.

We analyzed the dose-dependent effects of osmotic shifts on the dynamic parameters of the interphase MTs. We detected a progressive increase in the time that MTs spent in a pause state

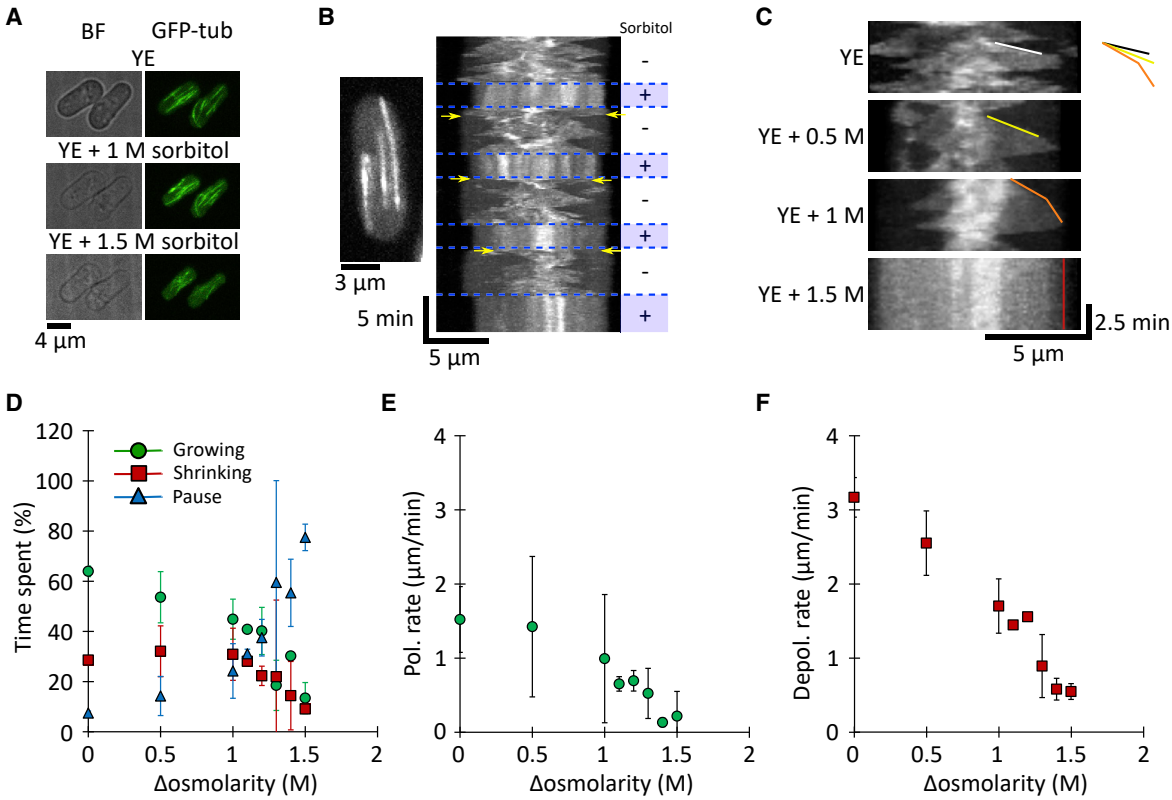

Figure 1. MT growth and shrinkage rates decrease upon hyperosmotic shock in yeast cells

(A) Brightfield (BF; left) and fluorescence (right) images of interphase MT bundles in two fission yeast cells expressing GFP-alpha tubulin 2 (GFP-tub) upon sequential treatment with YE (medium alone), YE + 1 M sorbitol, and YE + 1.5 M sorbitol.

(B) MT dynamics in a cell treated with oscillations of YE (5 min) and YE + 1.5 M sorbitol (3 min). In the kymograph, this representative cell is expressing GFP-tubulin; the cell image has been collapsed onto a line. MTs exhibit decreased dynamics acutely in 1.5 M sorbitol. Upon sorbitol washout, MTs first depolymerize (yellow arrows) and then resume dynamic behaviors.

(C) Kymographs of MTs in yeast cells at the indicated sorbitol concentrations. Lines highlight tracks of single growing MT plus ends. Colored lines highlight growth events.

(D) Percentage of time that interphase MTs spent growing (green circles), shrinking (red squares), or paused (blue triangles) in YE and after hyperosmotic shocks (average (AVG) ± standard deviation). Cell and MT values of n are as in (E).

(E) MT polymerization rates (green circles) in yeast cells treated acutely with the indicated sorbitol concentrations. Values are AVG ± standard deviation. n = 58/51/32/27/38/23/15/26 cells and 118/99/60/65/72/34/22/44 MTs (left to right on plot), from at least two experiments.

(F) MT depolymerization (red squares) rates in yeast cells treated acutely with the indicated sorbitol concentrations. Values are AVG ± standard deviation. Cell and MT values of n are as in (E). See Videos S1 and S2.

(Figure 1D). Without sorbitol, MTs spent 7 ± 1% of the time in pause, while at 1 M and 1.5 M sorbitol, they spent 24 ± 11% and 77 ± 5% of the time in pause, respectively (Figure 1D). Of the MTs that continued to be dynamic, their rates of polymerization and depolymerization decreased in a sorbitol dose-dependent manner (Figures 1C, 1E, 1F, and S3; Video S2). Importantly, sorbitol's effects on MT polymerization and depolymerization were equivalent in magnitude, a point to which we will return later. For instance, at 1.5 M sorbitol, polymerization and depolymerization rates decreased by −79 ± 2% and 80 ± 1%, respectively (Figures 1E and 1F). Because both polymerization and depolymerization rates were affected, we can rule out a mechanism based on changes in the concentration of tubulin, which should affect polymerization only. Treatment with high sorbitol concentrations also made MTs resistant to depolymerization at cold temperatures (Figure S4), further indicating that these MTs were in a highly stabilized state.

We next asked whether hypoosmotic shifts, which dilute the cytoplasm by causing an influx of water, yield opposite effects on MT dynamics. Our initial attempts to swell intact fission yeast cells with hypoosmotic shifts were not successful, perhaps because the cell wall limited the swelling. However, the cell wall can be removed enzymatically to create protoplasts, which swell substantially in response to hypoosmotic shifts without lysing (Figure 2A) (Lemière and Berro, 2018). To establish a control condition for protoplasts, we determined that protoplasts produced in 0.4 M sorbitol in rich media had the same average volume as intact fission yeast cells. Shifting the protoplasts to hypoosmotic and hyperosmotic conditions (relative to the isotonic condition of 0.4 M sorbitol) led to predictable changes in cell volume over a ~2.5-fold range (Figure 2A). MTs were readily imaged across all volumes (Figure 2B). In hypoosmotic shifts, MT polymerization and depolymerization rates both increased by an equivalent magnitude (Figures 2C–2F). For

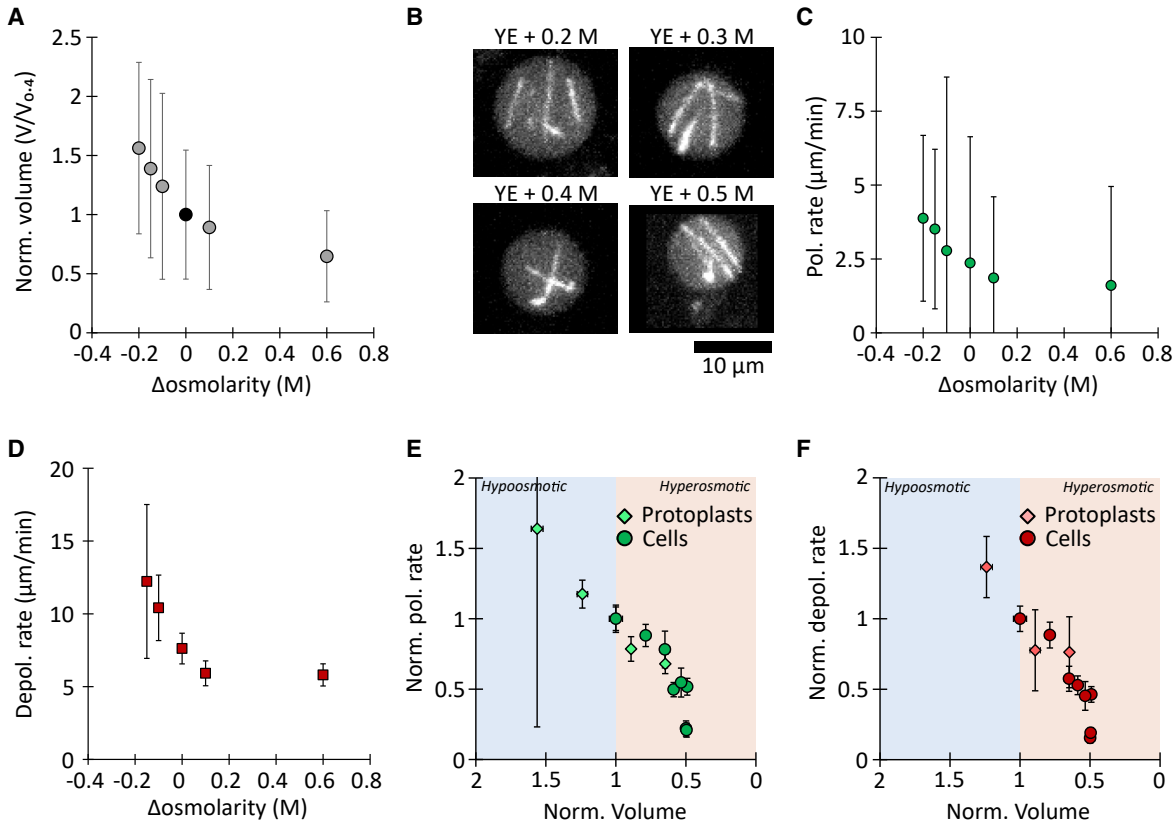

Figure 2. MT growth and shrinkage rates scale with cell volume in yeast protoplasts

(A) Normalized protoplast volume. Data were normalized to osmolarity conditions of YE + 0.4 M sorbitol, in which the average volume distribution of protoplasts matched that of intact cells (AVG ± standard deviation). Data come from at least two experiments; (left to right) n = 18/45/109/446/200/440 protoplasts.

(B) Representative images of GFP-labeled MTs in protoplasts in a medium supplemented with the indicated sorbitol concentrations.

(C) MT polymerization (Pol.) and (D) depolymerization (Depol.) rates in yeast protoplasts in a medium supplemented with the indicated sorbitol concentrations. Values are AVG ± standard deviation. Left to right, n = 10/13/64/29/28/25 polymerization events and n = 7/57/25/13/12 depolymerization events from three experiments.

(E) MT polymerization rate and (F) depolymerization rates, normalized to the isotonic condition for yeast cells (circles) and yeast protoplasts (diamonds), as a function of the normalized volume (see STAR Methods). Both rates increase in hypo-tonic conditions (blue shading) and decrease in hyper-tonic conditions (orange shading).

example, when cell volume swelled by 56 ± 1% over isotonic conditions, polymerization rates increased by 64 ± 3% and depolymerization rates increased by 42 ± 1% relative to control (Figures 2E and 2F). Conversely, hyperosmotic shifts in protoplasts decreased the rates of MT polymerization and depolymerization, also with equivalent magnitudes, similar to what was observed in intact fission yeast cells (Figures 2C–2F). This result implies that the properties of the cytoplasm dampen the rates of MT polymerization and depolymerization.

To evaluate whether intracellular concentration sets the rates of dynamic instability in other cell types, we performed similar osmotic shifts with the moss *Physcomitrium (Physcomitrella) patens* and mammalian Ptk2 cells. In both cases, we observed lower MT polymerization and depolymerization rates after hyperosmotic shifts, similar to what we observed in fission yeast (Figures 3 and S2). In Ptk2 cells (Figure 3; Video S3) treated with DMEM + 0.25 M sorbitol, MT polymerization rate decreased from 4.9 ± 1.5 µm/min to 2.4 ± 0.8 µm/min (−48%) while depolymerization rate decreased from 12 ± 3.4 µm/min to 6 ± 2.5 µm/min (−50%) (mean ± standard deviation). In moss cells (Figures S2; Video S3) treated with BCD + 0.5 M sorbitol, MT polymerization rate decreased from 5 ± 1 µm/min to 4 ± 0.7 µm/min (−20%) while depolymerization rate decreased from 30 ± 19 µm/min to 22 ± 15 µm/min (−28%) (mean ± standard deviation). The similar effects of osmotic shifts on MT in fungal, plant, and mammalian cells suggest that they arise from a conserved mechanism.

Normalization of the MT polymerization and depolymerization rates to the isotonic conditions for both yeast cells and protoplasts revealed how changes in the concentration of the cytoplasm, above and below normal levels, caused similar, linear responses for MT polymerization and depolymerization (Figures 2E and 2F). This response suggests that the property of the cytoplasm that is changed by osmotic shocks affects both MT polymerization and depolymerization in a similar manner. Interestingly, MT dynamics decreased when cytoplasmic density and tubulin concentration increased (Figures 1 and 2), opposite to what would be expected if crowding or tubulin concentration

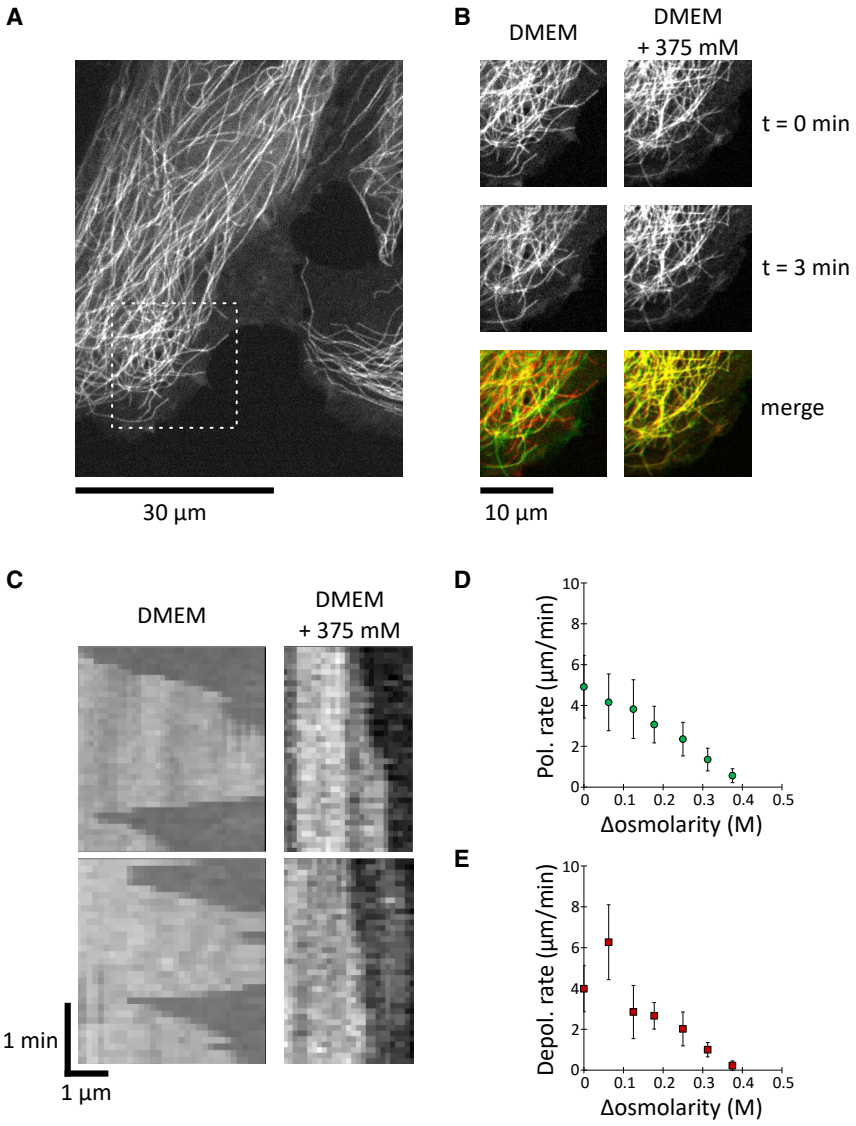

Figure 3. MT growth and shrinkage rates decrease upon hyperosmotic shock in mammalian cells

(A) Representative images of Ptk2 cells stably expressing GFP-labeled tubulin. Dashed boxed ROI is zoomed-in in (B).

(B) Snapshots from the cell in (A) showing MT dynamics before and after an osmotic shock with DMEM/F12 media containing 375 mM of sorbitol.

(C) Kymographs of MTs in Ptk2 cells at the indicated sorbitol concentrations.

(D) MT polymerization rates (green circles) in Ptk2 cells treated acutely with the indicated sorbitol concentrations. Values are AVG ± standard deviation. Data come from (left to right) n = 39/58/59/48/57/61/40 MT, from at least three cells and two experiments.

(E) MT depolymerization rates (red squares) in Ptk2 cells treated acutely with the indicated sorbitol concentrations. Values are AVG ± standard deviation. Data come from (left to right) n = 29/47/49/48/47/41/24 MT, from at least three cells and two experiments. See Video S4.

were responsible for the observed changes in MT dynamics as MT polymerization increases with either of these parameters (Wieczorek et al., 2013).

Effect of osmotic shifts on MT dynamics is independent of stress response and regulatory proteins at MT plus ends

Hyperosmotic shocks could influence MTs directly, through their effect on cytoplasm physical properties (such as concentration), or indirectly, e.g., through osmotic stress response pathways. We next investigated several plausible mechanisms for these effects of the cytoplasm on MT dynamics. To distinguish between direct and indirect mechanisms, we considered two indirect mechanisms: (1) osmotic stress response pathways (such as regulation through phosphorylation) and (2) regulation by MT regulators at the MT plus end.

First, we tested whether MT stabilization is a downstream effect of an osmotic stress response pathway. Cells respond to osmotic stress by activating protein kinases that alter metabolism and gene expression(Hohmann, 2002). The MAP kinase Sty1 (Hog1, p38 ortholog) is a master integrator of multiple stress pathways (Pérez and Cansado, 2010). However, in *sty1*Δ cells, sorbitol-mediated hyperosmotic shifts still caused a dampening of MT dynamics (Figure S3), as previously observed (Robertson and Hagan, 2008), and in fact, had slightly more severe effects than in (wild-type) WT cells. Other triggers of the Sty1 stress pathways, such as latrunculin A, do not produce MT "freezing" (Daga et al., 2006; Mutavchiev et al., 2016). Thus, "freezing" of the MT network is not a downstream response of Sty1-dependent stress pathways.

We next explored the role of MT regulatory proteins at MT plus ends (+TIPs), such as MT polymerases and depolymerases. +TIPs could be affected by osmotic shifts through Sty1-independent pathways that alter their activities, affinities, phosphorylation states, etc. In fission yeast, the major classes of +TIPs are represented by the EB-family protein Mal3, the XMAP215-family MT polymerase Alp14 (XMAP215), and the kinesin-8 complex Klp5/6 (Akhmanova and Steinmetz, 2010; Al-Bassam et al., 2012; Busch and Brunner, 2004; Unsworth et al., 2008). In *mal3Δ*, *alp14Δ*, *tip1Δ*, and *klp5Δ* mutants, hyperosmotic shifts caused a dampening of MT dynamics similar to that observed in WT cells (Figure S4). Therefore, the dampening is not dependent on these individual +TIPs proteins. Additionally, because Mal3 is required for the recruitment of many other +TIP proteins (Akhmanova and Steinmetz, 2010), the *mal3Δ* mutant causes general disruption of the +TIP network—yet, MT polymerization and depolymerization still "froze" during hyperosmotic shifts. We next asked how hyperosmotic shifts impacted the localization of +TIPs. We observed that

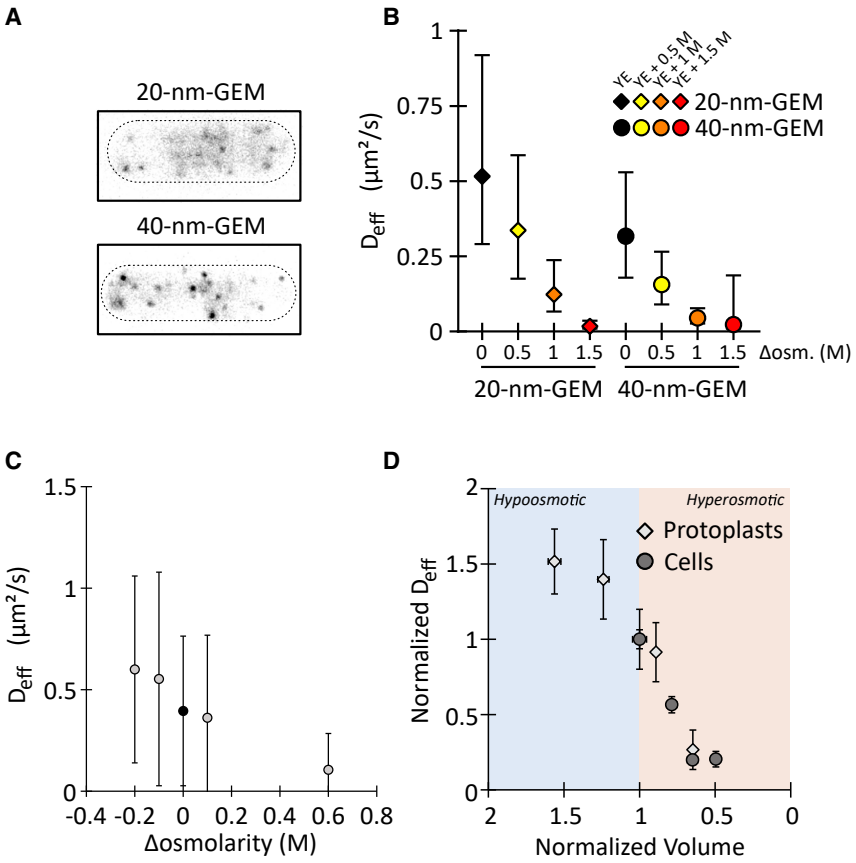

Figure 4. Nanoparticle's diffusion rate scales with cytoplasm concentration

(A) Representative images of GEMs in fission yeast cells. Scale of box width is 5 μm.

(B) Hyperosmotic shifts decrease the effective diffusion coefficients of GEMs of indicated sizes in yeast cells. Values are AVG ± standard deviation. Data come from three experiments, n > 1,000 trajectories, and n > 49 cells. Concentrations reflect sorbitol concentrations in the medium.

(C) Effective diffusion coefficients of 40-nm GEMs in yeast protoplasts as a function of sorbitol. AVG ± standard deviation. Data come from at least two experiments and (left to right) n = 643/411/304/488/162 trajectories.

(D) Diffusion rate of the 40-nm GEMs in yeast cells (circles) and yeast protoplasts (diamonds) normalized to the iso-tonic condition as a function of the normalized volume (see STAR Methods). The rate of diffusion through the cytoplasm is faster in hypotonic conditions (blue shading) and slower in hypertonic conditions (orange shading). See Video S5.

Alp14-GFP was maintained at the MT plus ends during hyperosmotic shifts; in contrast, Mal3-GFP localization at MT plus ends decreased (Figure S4). As Mal3 localization is dependent on the nucleotide binding state of tubulin (Maurer et al., 2011, 2012; Guesdon et al., 2016), this loss of Mal3 may signify the loss of the GTP cap during the period when MTs are "frozen", consistent with the prompt catastrophes we observed following the reversal of hyperosmotic shifts (Figures 1B and S1).

Taken together, our observations in mutant cells argue that the acute effect of hyperosmotic shocks on MT dynamics observed here is not caused by indirect mechanisms such as the osmotic stress response or MT regulators. Rather, MT polymerization and depolymerization may be directly affected by the physical properties of the cytoplasm.

Cytoplasmic properties modulate the motion of nanoparticles

To understand how cytoplasmic properties could affect a biochemical reaction like MT polymerization, we next set out to physically characterize the cytoplasm of fission yeast cells and examine how changes upon osmotic shifts affect MT dynamics. We reasoned that if the cytoplasm affects MTs through physical means, then it should also affect other intracellular components not related to MTs. First, we performed nanorheology experiments to assess the effects of the cytoplasm on diffusive-like motion of nanoparticles that have the similar size scale as large macromolecules. As probes, we used genetically encoded multimeric proteins (GEMs) that assemble into spherical nanoparticles of defined sizes (Delarue et al., 2018). We expressed GEMs tagged with the fluorescent protein sapphire in fission yeast (STAR Methods) and imaged them at 100 fps to analyze their motion (Figure 4A). We analyzed 20- and 40-nm diameter GEMs, which are similar in size as ribosomes and of similar scale to the diameter of the MT plus end (Delarue et al., 2018). Mean squared displacement (MSD) plots revealed that the movements of the GEMs were sub-diffusive (anomalous diffusion exponent α <1) (Figure S5), as observed in other cell types (Delarue et al., 2018), consistent with motion being restricted by a heterogeneous meshwork of organelles and macromolecules (Luby-Phelps et al., 1986). Their diffusive-like motion at short timescales allowed us to estimate the effective diffusion coefficient (D_{eff}) (see STAR Methods and Delarue et al. 2018). GEM D_{eff} was size dependent: larger GEMs (40 nm, D_{eff} = 0.33 ± 0.14) diffused more slowly than the smaller GEMs (20 nm, D_{eff} = 0.53 ± 0.23) (Figure 4B; Video S5), consistent with previous rheological observations in other cell types (Luby-Phelps et al., 1986; Moeendarbary et al., 2013). Thus, the cytoplasm of fission yeast appears broadly similar to the cytoplasm from other eukaryotes. Interestingly, the effective diffusion coefficient of the 40-nm GEM in fission yeast (~0.3 $\mu m^2/s$) is similar to what was reported in budding yeast (~0.3 $\mu m^2/s$) but slower than that in mammalian cells (~0.5 $\mu m^2/s$) (Delarue et al., 2018), revealing possible intrinsic differences in the level of crowding or the structure of the cytoplasm among these cell types.

Having characterized GEM diffusion in untreated cells, we then measured the impact of osmotic shifts on the diffusion of the two different sized particles. As expected, the impact was size dependent. At 1 M sorbitol, 40-nm GEMs were effectively immobile, while 20-nm GEMs still diffused detectably (Figure 4B). At 1.5 M sorbitol, GEMs of both sizes were effectively immobile (Figure 4B).

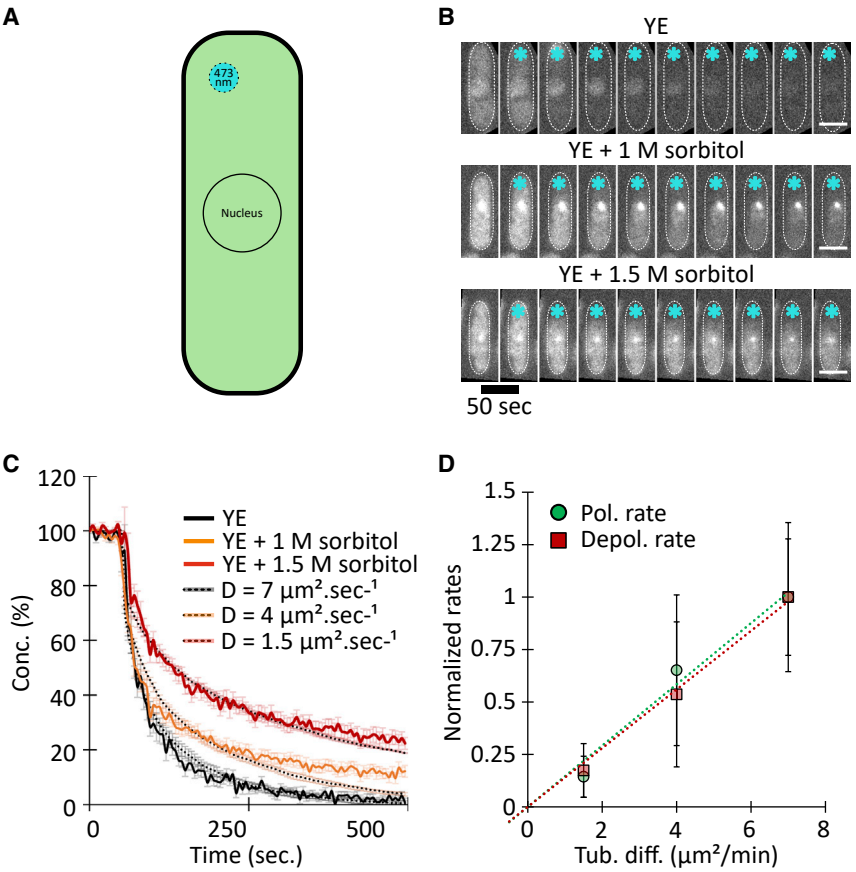

Figure 5. Hyperosmotic shifts decrease the diffusion rate of soluble tubulin

(A) To measure the diffusion of soluble GFP-tubulin, we used FLIP. Cells were exposed repeatedly to a focused laser beam (~1 μm) near one cell tip, and GFP fluorescence intensity was measured (see STAR Methods).

(B) Fluorescence decay of cells expressing GFP-tubulin in a representative FLIP experiment after hyperosmotic shock at the indicated sorbitol conditions. Interphase cells in which MTs were depolymerized with 25 μg/ml methyl benzimidazol-2-yl-carbamate (MBC) were photobleached using a focused laser (blue stars). Scale bars, 4 μm.

(C) Loss of fluorescence intensity in cells from three osmotic conditions and the corresponding tubulin diffusion rate. Values (AVG ± standard deviation) were normalized to initial intensity and expressed as concentrations (%). Data are n = 46, 29, and 29 cells for YE alone, YE + 1 M sorbitol, and YE + 1.5 M sorbitol, respectively, from three independent experiments. Dashed lines denote predictions from simulations of a 1D model (see STAR Methods) for various values of diffusion; these predictions were used to estimated diffusion rates from our experimental data. Simulation values are AVG ± standard deviation for five simulations.

(D) Rates of MT polymerization and depolymerization in yeast cells as a function of tubulin diffusion rate. Data come from Figures 1 and 4. Correlations between diffusion and polymerization rate ($p = 0.008$) and depolymerization rate ($p = 0.001$) are significant according to Pearson's correlation test.

To compare the effects of hypoosmotic and hyperosmotic shifts, we next analyzed GEMs in protoplasts. To establish the baseline osmolarity, we confirmed that at 0.4 M sorbitol, D_{eff} values for GEMs in protoplasts were similar to those in cells with intact cell walls (Figure 4C), indicating that this sorbitol concentration is the isotonic point, consistent with volume measurements. Hypoosmotic shifts increased D_{eff}, while hyperosmotic shifts decreased D_{eff} (Figure 4C). Despite the potential complexity of the cytoplasm, these GEMs data showed that the diffusion of GEMs scaled inversely with cytoplasm concentration (Figure 4D). Comparison of GEM D_{eff} and MT rate data (Figures 2E, 2F, and 4D) showed the same general trend that they all scaled inversely with cytoplasmic concentration. These observations in yeast cells and protoplasts suggest that the physical properties of cytoplasm change with cytoplasm concentration in ways that alter the diffusion of spherical particles such as GEMs as well as MT dynamics.

Microtubule dynamics scale with tubulin diffusion in cells

We next directly assessed the effects of osmotic shifts on the diffusion of soluble αβ-tubulin. We measured the diffusion of soluble tubulin by fluorescence loss in photobleaching (FLIP) experiments. In FLIP, the fluorescence intensity in a whole cell is measured while a small region of the cytoplasm is repeatedly photobleached. The rate at which whole-cell fluorescence decreases over time can be used to estimate the diffusion coefficient of a fluorescent protein (Figure 5A; Ishikawa-Ankerhold et al., 2012). As a probe for soluble α/β-tubulin dimers, we used Atb2-GFP (α-tubulin 2) expressed from the native chromosomal locus (Sato et al., 2009). To prevent MT polymers from confounding the measurement, cells were treated with the MT inhibitor methyl benzimidazol-2-yl-carbamate (MBC) to depolymerize MTs (Figure 5B). To estimate the tubulin diffusion coefficient from the continuous loss of fluorescence, we designed a 1D stochastic model of tubulin diffusion that assumes a single diffusing species (STAR Methods). Comparison of the model predictions with our experimental data (Figure 5B) yielded an estimated diffusion coefficient of GFP-tubulin of D = 7 $\mu m^2\ s^{-1}$ in control cells, which is very close to the value of ~6 $\mu m^2\ s^{-1}$ obtained in pioneering experiments in sea urchin (Salmon et al., 1984) and in PTK2 cells (Wang et al., 2004). In cells treated with hyperosmotic shifts, the estimated diffusion coefficient of soluble tubulin decreased to D = 4 $\mu m^2\ s^{-1}$ at 1 M sorbitol and D = 1.5 $\mu m^2\ s^{-1}$ at 1.5 M sorbitol (Figure 5C). A linear relationship emerged, where both the MT polymerization and depolymerization rates correlated linearly with the tubulin diffusion coefficient (Figure 5). Taken together, these data suggest that tubulin diffusion is modulated by the physical properties of the cytoplasm and is likely to contribute to the observed changes in MT polymerization and depolymerization rates upon osmotic shifts.

Cytoplasm viscosity increases in hyperosmotic shifts

In the ideal models of diffusion, namely the purely Brownian motion of a spherical particle in solution, the diffusion coefficient

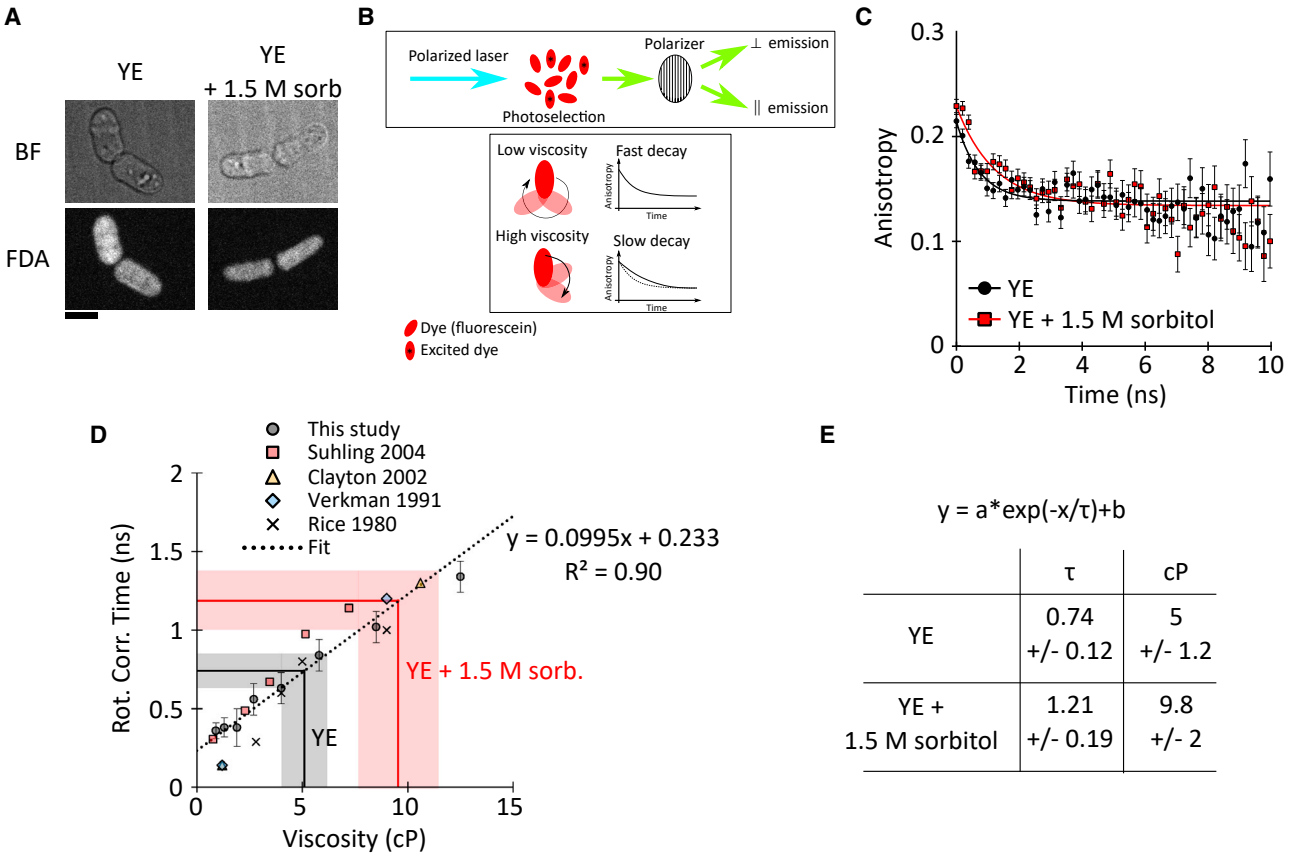

	τ	cP
YE	0.74 +/- 0.12	5 +/- 1.2
YE + 1.5 M sorbitol	1.21 +/- 0.19	9.8 +/- 2

Figure 6. Hyperosmotic shocks increase the viscosity of the cytoplasm in yeast

(A) Image of cells labeled with 100 μM fluorescein diacetate (FDA) in YE and YE + 1.5 M sorbitol. Bar represents 5 μm.

(B) Schematic illustrating the principle of the time-resolved fluorescence anisotropy imaging (TR-FAIM) experiment.

(C) Anisotropy decay of fluorescence in wild-type fission yeast cells in YE media (black circles) and YE + 1.5 M sorbitol (red squares) (AVG ± standard deviation). The black and red plain lines represent the best fits. Differences are significant according to a F-test, p value = 0.0003.

(D) Calibration plot of fluorescein rotational correlation time in solution of different viscosity. Data from this study (black circles) and others were used. The linear regression represents the best fit. The equation was used to convert the rotational correlation time from the fits in (B) to viscosity estimates.

(E) Summary of the viscosity values obtained in yeast cell in YE and YE + 1.5 M sorbitol.

scales (1) linearly with the temperature, (2) inversely with the radius of the particle, and (3) the dynamic viscosity of the solution (Einstein, 1905). Because intracellular diffusion is complex and potentially driven by active processes, we sought to test whether viscosity of the cytoplasm changes with its concentration. We estimated fluid-phase viscosity of the fission yeast cytoplasm using time-resolved fluorescence anisotropy imaging (tr-FAIM) (Siegel et al., 2003). This method measures the Brownian rotational movement of a fluorescent dye (fluorescein) in the cytoplasm of living cells, assessing viscosity at the Ångström size scale of the dye (see STAR Methods; Figure 6). Higher viscosity leads to a lower rotation rate of the dye and slower depolarization (Figure 6B). Fitting and extraction of the rate constants (Figure 6C) and comparison to the calibration curve (Figure 6D) yielded an effective viscosity value at 22°C of 5 ± 1.2 cP (Figure 6E), which is in line with the broad range of previous viscosity measurements for eukaryotic cytoplasm (range: 1–50 cP) (Obodovskiy, 2019). This value suggests that at 22°C, the fission yeast cytoplasm has an effective viscosity value similar to that of 43% (v/v) glycerol in water. For cells treated with 1.5 M sorbitol, the effective viscosity of the cytoplasm was 9.8 ± 2 cP (Figure 6E), corresponding to 54% (v/v) glycerol in water at 22°C. Thus, the effective viscosity of the cytoplasm increases with its concentration upon a hyperosmotic shift, qualitatively consistent with the effects on translational diffusion rates of GEMs and tubulin dimers.

Viscosity is sufficient to explain the effects of cytoplasmic concentration

In order to isolate the effects of viscosity on MT dynamics, we reconstituted MT dynamics *in vitro* in the presence of glycerol using a well-established assay (Gell et al., 2011; Figure 7A). Glycerol is a small molecule that increases viscosity in the solution without significant crowding effects. Although glycerol has been long known to stabilize MTs in bulk (Keates, 1980), its inhibitory effects on the growth rate of individual MTs *in vitro* were only recently shown (Wieczorek et al., 2013). However, the effect of glycerol on MT depolymerization has not been analyzed. We took advantage of interference reflection microscopy (IRM) (Mahamdeh and Howard, 2019) to image MTs at 0.5 fps for extended

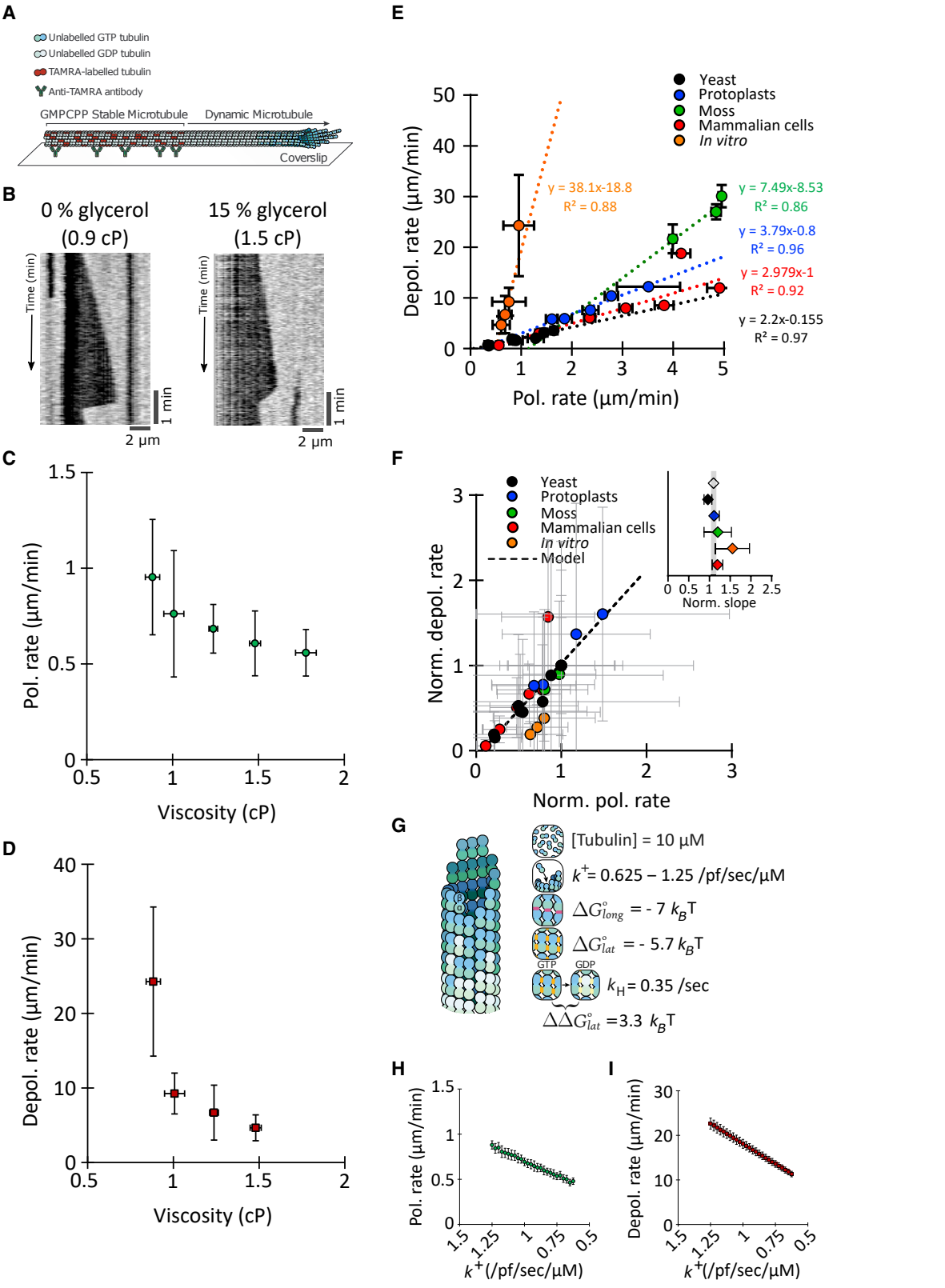

(legend on next page)

periods, allowing a more accurate quantification of depolymerization rates as compared with imaging fluorescently labeled MTs. A range of glycerol concentrations was added to the reconstitutions to produce viscosities from 0.9 to 1.9 cP. MT polymerization rates decreased linearly in a dose-dependent manner with increasing viscosity, similar to what was previously shown (Wieczorek et al., 2013; Figure 7C). Strikingly, MT depolymerization rates also decreased with glycerol addition (Figure 7D; Video S5). As high glycerol concentrations (>20%) suppressed catastrophe under these conditions, we further probed the effect of glycerol on MT depolymerization using a buffer exchange system to induce catastrophe by removing free tubulin (see STAR Methods). These experiments recapitulated the inhibitory effects of glycerol on MT depolymerization rates and showed that MT depolymerization was largely abolished at 30%–40% glycerol concentrations (Figure S10; Video S6), reminiscent of the frozen MTs observed in cells. Thus, the influence of cytoplasmic properties on MT polymerization and depolymerization rates observed *in vivo* was reproduced *in vitro* by modulating a single parameter, viscosity.

To compare these *in vitro* results with the *in vivo* findings quantitatively, we plotted depolymerization rates as a function of polymerization rate for all the conditions we studied (Figure 7E). Our *in vivo* and *in vitro* experiments paint a consistent picture: rates of MT polymerization and depolymerization are linearly correlated, indicating a conserved ratio of polymerization to depolymerization (Figure 7E). The ratio is different in each experimental case, presumably due to the specific conditions of each case (active cytoplasm versus *in vitro* reconstruction, presence of MAPs, tubulin isoform properties, tubulin concentration, temperature, etc.). Nonetheless, the ratio is maintained when MT dynamics are perturbed, either by changes in cytoplasm concentration *in vivo* or changes in viscosity *in vitro*. By normalizing the rates from each model to the value in the unperturbed condition, all of the data from *in vivo* and *in vitro* experiments strikingly collapsed onto the same slope (Figure 7F). This relationship shows that viscosity and the concentration of the cytoplasm affect a fundamental, conserved property of MT polymerization and depolymerization in a similar manner.

Using a 6-parameter model for MT dynamic instability (Figure 7G) (Hsu et al., 2020) that reproduces the core behaviors of polymerization, catastrophe, and depolymerization (Odde, 1997), we could reproduce these data by modulating the tubulin association rate constant k^+ as a proxy for the effect of viscosity. Indeed, the parameter k^+ defines the rate at which intermediate complexes form. This rate will be reduced by viscosity, because viscosity limits molecular motion. All other parameters, notably the ΔGs of tubulin-tubulin bonds, remained constant. The model predicts that polymerization rates decrease in a linear manner with decreasing k^+, as expected from fewer binding events (Figure 7H). Notably, the model also predicts that depolymerization rates also scale linearly with k^+ (Figure 7I) because when association rate constants change, dissociation rate constants must also change if the bond energies (ΔG_{long} and ΔG_{lat}) are to remain constant (Drenckhahn and Pollard, 1986). In other words, the model predicts that both rates scale linearly with the association rate constant, explaining the collapse of the normalized data on a single slope (Figure 7F). Thus, this initial model shows how an increase in viscosity that causes slower molecular motion can decrease both polymerization and depolymerization rates proportionally without affecting the bond energies. Thus, MT dynamic instability in the cytoplasm is modulated by a single master variable, which is viscosity.

Hyperosmotic shift dampens mitotic spindle elongation and DNA segregation

As a demonstration that this regulation by cytoplasmic properties affects an MT-dependent process *in vivo*, we determined how osmotic shifts affect the functioning of the mitotic spindle during anaphase. The fission yeast anaphase spindle is inside the nucleus and is composed of a single MT bundle that elongates by MT polymerization and slides to move the chromosomes apart (Krüger et al., 2019). We imaged mitotic cells expressing GFP-tubulin and mCherry-histone during oscillatory hyperosmotic shocks of 1 M or 1.5 M sorbitol (similar to Figure 1B). These conditions have been shown to reduce GEM diffusion in the nucleoplasm to a similar extent as they do in the cytoplasm (Lemière et al., 2021). During each 5-min period of sorbitol treatment, the rates of spindle elongation abruptly decreased; elongation rate decreased by around half in the 1 M sorbitol shift and completely stopped at 1.5 M sorbitol (Figure S7; Video S7). Remarkably, upon each shift back to normal media, the spindle promptly

Figure 7. Increasing viscosity dampens rates of MT polymerization and depolymerization similarly

(A) Schematic of the *in vitro* reconstituted system for MT dynamics measurement.

(B) Representative kymographs of MTs grown in BRB80 and BRB80 + 15% glycerol to increase the viscosity. Polymerization and depolymerization rates are slower at higher viscosity.

(C and D) (C) MT polymerization rates (green circles) and (D) MT depolymerization rates (red squares) were measured in MTs in solutions of varying viscosity. Data represent three repetitions with n ≥ 70 MTs per condition.

(E) Scatter plot of the observed depolymerization rates versus the observed polymerization rates for the experiments in this study (yeast cells [black circles], yeast protoplasts [blue circles], moss [green circles], ptk2 cells [red circles], and *in vitro* [orange circles]). Each model presents a certain ratio (the slope of the regression) of depolymerization rate to polymerization rate, but this ratio (the slope) is conserved when viscosity is increased *in vitro* and when cytoplasm concentration is manipulated by osmotic shocks (yeast, protoplasts, moss, and Ptk2 cells) *in vivo*. AVG ± SEM (for some data points, the error bars are smaller than the point).

(F) Cytoplasm and viscosity have similar effects of MT polymerization and depolarization rates. Graph shows the relationship between normalized depolymerization rates and normalized polymerization rates for all the experimental conditions and for the model, described in (C). AVG ± propagated error. All the systems (yeast, protoplast, moss, Ptk2, and *in vitro*) have the same slope as the model (see STAR Methods). The inlet shows the slope obtained from each dataset (AVG ± STD) and the slope from the model as a grayed area.

(G) Schematic of the parameters used to model MT dynamic instability. Changing the association rate constant k^+ was used to model the effect of viscosity. For more details, see STAR Methods.

(H and I) (H) Polymerization rate (apparent on-rate) and (I) depolymerization rate (apparent off-rate) as a function of the association rate constant in the model. Note that the x axis is inverted. See Videos S5 and S6.

resumed elongating at similar rates before the shift, without apparent MT loss or change in spindle organization; despite intermittent pauses, the vast majority of these cells completed anaphase successfully. For the 1.5 M shifts, the duration of mitosis increased roughly by the time the spindle was frozen (Figure S11H). These effects on anaphase B rates may reflect the effects of varying cytoplasmic viscosity on MT dynamics, motor function, and possible drag forces in moving the micron-scale nuclei through the cytoplasm. Our findings illustrate how cytoplasmic properties dictate the rate of biological processes.

DISCUSSION

Here, we used MT dynamics as a model reaction to study how the physical properties of the cytoplasm influence biochemical reactions. During hyperosmotic shifts that increase cytoplasmic concentration, MTs polymerized and depolymerized more slowly and paused more frequently (Figure 1). Conversely, in hypoosmotic conditions, which decreases cytoplasmic concentration, MT polymerization and depolymerization rates sped up as much as 50% (Figure 2). We provide numerous lines of evidence to indicate that these effects act directly via the physical properties of the cytoplasm, as opposed to an indirect mechanism via osmotic stress pathways or MT regulatory proteins Figures S1). The effects were rapid (Figure 1), reversible (Figure S1), and scaled linearly with the concentration of cytoplasm in hypoosmotic and hyperosmotic shocks (Figure 2), strongly indicative of a physical response. The effects on MTs scaled with effects on the diffusive motion of GEMs and tubulin dimers (Figures 4 and 5). A significant implication is that cytoplasm properties, such as its viscosity, set the rates of MT polymerization and depolymerization at physiological conditions. Additionally, using osmotic shocks on Ptk2 cells (Figure 3) and on moss cells (Figure S2), we obtained similar results, suggesting that the effect of the cytoplasm concentration on MT dynamics is conserved across eukaryotes. Furthermore, we can reproduce the effect of cytoplasm concentration on MTs grown *in vitro* by increasing the viscosity of the buffer (Figure 7). Our findings further indicate that the predominant impact of cytoplasmic concentration on MTs is through its viscosity, rather than effects of macromolecular crowding or changes in tubulin concentration. Indeed, these findings provide one of the first demonstrations of how the viscosity of the cytoplasm impacts an endogenous intracellular reaction.

Viscosity is likely to impact a multitude of biochemical reactions and multi-scale conformational dynamics that drive the polymerization and depolymerization of MTs (Brouhard and Rice, 2018). For MT polymerization, viscosity may inhibit diffusive arrival and positioning of a curved, GTP-tubulin dimer to the end of a protofilament (Figure 5). Viscosity may affect the subsequent steps in which tubulin dimers straighten and form bonds between the full complement of neighboring dimers, as well as changes in protofilament conformation during assembly of the MT lattice. For MT depolymerization, viscosity may affect the large conformational changes in protofilaments as they peel away from the MT end to form curved structures. These structural transitions, which involve significant changes in tertiary and quaternary structures (Brouhard and Rice, 2018), are influenced by solvent interactions and hence, potentially by changes in viscosity. These transitions may be affected differently by different agents depending on their size scale (Sozański et al., 2015; Wieczorek et al., 2013). Additional studies will be needed to determine the specific rate-limiting reactions of MT dynamics and organization responsible for these effects of viscosity.

In summary, we used MT dynamics as an example to study how the physical properties of the cytoplasm affect biochemical reactions *in vivo* and discovered that viscosity plays a key role. This works highlights the impact of cytoplasmic viscosity on the rates of intracellular reactions and may generalize to diverse processes including kinesin function (Sozański et al., 2015), actin polymerization (Drenckhahn and Pollard, 1986), the assembly of multi-subunit complexes such as protein aggregation or amyloid formation (Munishkina et al., 2004), and the folding of proteins and RNA (Dupuis et al., 2018; Hagen, 2010; Pradeep and Udgaonkar, 2007), as well as signaling (Miermont et al., 2013). The density and other properties of the cytoplasm are known to vary during the cell cycle, in development, aging, and diseases (Neurohr and Amon, 2020). Recent findings in budding yeast suggest that cytoplasmic viscosity itself may be actively regulated through regulation of metabolites such as trehalose and glycogen, for instance, in response to environmental conditions such as temperature changes (Persson et al., 2020). The dynamic of the cytoskeleton may also contribute to regulation of the cytoplasm properties (Charras et al., 2009; Fakhri et al., 2014; Guo et al., 2018), setting up a potential feedback loop. Therefore, it will be important to consider how physiological changes in cytoplasmic properties globally cross-talk with cytoskeletal elements, metabolism, and the many other cellular reactions in the living cell.

STAR★METHODS

Detailed methods are provided in the online version of this paper and include the following:

- KEY RESOURCE TABLE
- RESOURCE AVAILABILITY
  - Lead contact
  - Materials availability
  - Data and code availability
- EXPERIMENTAL MODEL AND SUBJECT DETAILS
  - Fission yeast
  - Physcomitrium (Physcomitrella) patens
  - Mammalian cells
- METHOD DETAILS
  - Yeast strain construction
  - Protoplast preparation
  - Imaging of fission yeast
  - Osmotic shock experiments
  - Measurements of MT dynamic parameters and cell volume in yeast and protoplasts
  - FLIP experiments
  - Microrheology with GEMs nanoparticles
  - MT dynamics in moss cells
  - MT dynamics in mammalian cells
  - MT dynamics *in vitro*
  - Cytoplasmic viscosity measurements
  - Normalizations

SUPPLEMENTAL INFORMATION

Supplemental information can be found online at https://doi.org/10.1016/j.devcel.2022.02.001.

ACKNOWLEDGMENTS

We thank members of the Chang Lab and Sophie Dumont and her lab for fruitful discussions. We are grateful to Dr. Rikki Garner for countless discussions and her help setting up the stochastic model of diffusion and to Dr. Fabrice Cordelières for the KymoToolBox ImageJ plug-in. We thank Sherman Foo and the Oliferenko Lab for reagents and technical support. We are grateful to Nikon for microscope support at MBL and to the MBL communities from the Physical Biology of the Cell Course, the Physiology Course, and the Whitman Investigator Program for support and advice. This work was supported by grants to F.C. (NIH GM115185, NIH GM056836, NIH GM146438), to L.J.H. (American Cancer Society RSG-19-073-01-TBE, Pershing Square Sohn Cancer Award, Chan Zuckerberg Initiative, NIH GM132447 and NIH CA240765), to G.G. (JSPS KAKENHI 17H06471 and 18KK0202), to K.S. (UK's Biotechnology and Biological Sciences Research Council (BBSRC) grant BB/R004803/1) and to M.T. (ERC Consolidator Grant 771599). I.E.S. was supported by King's College London through a LIDo (London Interdisciplinary Doctoral programme) iCASE studentship.

AUTHOR CONTRIBUTIONS

Conceptualization, A.T.M. and F.C.; methodology, A.T.M., J.L., M.G., C.H.E., C.-T.H., E.I.S., K.S., G.G., L.J.H., G.J.B., M.T., and F.C.; formal analysis, A.T.M., J.L., M.G., C.H.E., and E.I.S.; investigations, A.T.M., J.L., P.R.-C., C.H.E., and E.I.S.; writing, A.T.M., G.J.B., and F.C.; review editing, A.T.M., C.H.E., G.J.B., and F.C.; visualization, A.T.M.; supervision, A.T.M.; project administration and funding acquisition, F.C.

DECLARATION OF INTERESTS

The authors declare no competing interests.

INCLUSION AND DIVERSITY

One or more of the authors of this paper self-identifies as a member of the LGBTQ+ community.

Received: April 6, 2021
Revised: November 1, 2021
Accepted: January 31, 2022
Published: February 28, 2022

REFERENCES

Akhmanova, A., and Steinmetz, M.O. (2010). Microtubule +TIPs at a glance. J. Cell Sci. *123*, 3415–3419.

Al-Bassam, J., Kim, H., Flor-Parra, I., Lal, N., Velji, H., and Chang, F. (2012). Fission yeast Alp14 is a dose-dependent plus end-tracking microtubule polymerase. Mol. Biol. Cell *23*, 2878–2890.

Ashford, A.J., and Hyman, A.A. (2006). Preparation of tubulin from porcine brain. Cell Biology *2*, 155–160.

Atilgan, E., Magidson, V., Khodjakov, A., and Chang, F. (2015). Morphogenesis of the fission yeast cell through cell wall expansion. Curr. Biol. *25*, 2150–2157.

Bateman, J.B., Wagman, J., and Carstensen, E.L. (1966). Refraction and absorption of light in bacterial suspensions. Kolloid-ZuZPolymere *208*, 44–58.

Beauzamy, L., Nakayama, N., and Boudaoud, A. (2014). Flowers under pressure: ins and outs of turgor regulation in development. Ann. Bot. *114*, 1517–1533.

Brouhard, G.J., and Rice, L.M. (2018). Microtubule dynamics: an interplay of biochemistry and mechanics. Nat. Rev. Mol. Cell Biol. *19*, 451–463.

Busch, K.E., and Brunner, D. (2004). The microtubule plus end-tracking proteins mal3p and tip1p cooperate for cell-end targeting of interphase microtubules. Curr. Biol. *14*, 548–559.

Charras, G.T., Mitchison, T.J., and Mahadevan, L. (2009). Animal cell hydraulics. J. Cell Sci. *122*, 3233–3241.

Chowdhury, S., Smith, K.W., and Gustin, M.C. (1992). Osmotic stress and the yeast cytoskeleton: phenotype-specific suppression of an actin mutation. J. Cell Biol. *118*, 561–571.

Clayton, A.H.A., Hanley, Q.S., Arndt-Jovin, D.J., Subramaniam, V., and Jovin, T.M. (2002). Dynamic fluorescence anisotropy imaging microscopy in the frequency domain (rFLIM). Biophys. J. *83*, 1631–1649.

Daga, R.R., Yonetani, A., and Chang, F. (2006). Asymmetric microtubule pushing forces in nuclear centering. Curr. Biol. *16*, 1544–1550.

Delarue, M., Brittingham, G.P., Pfeffer, S., Surovtsev, I.V., Pinglay, S., Kennedy, K.J., Schaffer, M., Gutierrez, J.I., Sang, D., Poterewicz, G., et al. (2018). mTORC1 controls phase separation and the biophysical properties of the cytoplasm by tuning crowding. Cell *174*, 338–349.e20.

Drenckhahn, D., and Pollard, T.D. (1986). Elongation of actin filaments is a diffusion-limited reaction at the barbed end and is accelerated by inert macromolecules. J. Biol. Chem. *261*, 12754–12758.

Dupuis, N.F., Holmstrom, E.D., and Nesbitt, D.J. (2018). Tests of Kramers' theory at the single-molecule level: evidence for folding of an isolated RNA tertiary interaction at the viscous speed limit. J. Phys. Chem. B *122*, 8796–8804.

Edelstein, A.D., Tsuchida, M.A., Amodaj, N., Pinkard, H., Vale, R.D., and Stuurman, N. (2014). Advanced methods of microscope control using μManager software. J Biol Methods *1*, e10. https://doi.org/10.14440/jbm.2014.36.

Einstein, A. (1905). Über die von der molekularkinetischen Theorie der Wärme geforderte Bewegung von in ruhenden Flüssigkeiten suspendierten Teilchen. Ann. Phys. *322*, 549–560.

Ellis, R.J. (2001). Macromolecular crowding: obvious but underappreciated. Trends Biochem. Sci. *26*, 597–604.

Fakhri, N., Wessel, A.D., Willms, C., Pasquali, M., Klopfenstein, D.R., MacKintosh, F.C., and Schmidt, C.F. (2014). High-resolution mapping of intracellular fluctuations using carbon nanotubes. Science *344*, 1031–1035.

Flor-Parra, I., Zhurinsky, J., Bernal, M., Gallardo, P., and Daga, R.R. (2014). A Lallzyme MMX-based rapid method for fission yeast protoplast preparation. Yeast *31*, 61–66.

Fygenson, D.K., Braun, E., and Libchaber, A. (1994). Phase diagram of microtubules. Phys. Rev. E Stat. Phys. Plasmas Fluids Relat. Interdiscip. Topics *50*, 1579–1588.

Gell, C., Friel, C.T., Borgonovo, B., Drechsel, D.N., Hyman, A.A., and Howard, J. (2011). Purification of tubulin from porcine brain. Methods Mol. Biol. *777*, 15–28.

Guesdon, A., Bazile, F., Buey, R.M., Mohan, R., Monier, S., García, R.R., Angevin, M., Heichette, C., Wieneke, R., Tampé, R., et al. (2016). EB1 interacts with outwardly curved and straight regions of the microtubule lattice. Nat. Cell Biol. *18*, 1102–1108.

Guo, Y., Li, D., Zhang, S., Yang, Y., Liu, J.J., Wang, X., Liu, C., Milkie, D.E., Moore, R.P., Tulu, U.S., et al. (2018). Visualizing intracellular organelle and cytoskeletal interactions at nanoscale resolution on millisecond timescales. Cell *175*, 1430–1442.e17.

Hagen, S.J. (2010). Solvent viscosity and friction in protein folding dynamics. Curr. Protein Pept. Sci. *11*, 385–395.

Haupt, A., Ershov, D., and Minc, N. (2018). A positive feedback between growth and polarity provides directional persistency and flexibility to the process of tip growth. Curr. Biol. *28*, 3342–3351.e3.

Helenius, J., Brouhard, G., Kalaidzidis, Y., Diez, S., and Howard, J. (2006). The depolymerizing kinesin MCAK uses lattice diffusion to rapidly target microtubule ends. Nature *441*, 115–119.

Hohmann, S. (2002). Osmotic stress signaling and osmoadaptation in yeasts. Microbiol. Mol. Biol. Rev. *2*, 300–372.

Höög, J.L., Schwartz, C., Noon, A.T., O'Toole, E.T., Mastronarde, D.N., McIntosh, J.R., and Antony, C. (2007). Organization of interphase microtubules in fission yeast analyzed by electron tomography. Dev. Cell *12*, 349–361.

Hsu, C.-T., Brouhard, G.J., and Francois, P. (2020). Numerical parameter space compression and Its application to biophysical models. Biophys J *118*, 1455–1465.

Hyman, A.A. (1991). Preparation of marked microtubules for the assay of the polarity of microtubule-based motors by fluorescence. J. Cell Sci. Suppl. *14*, 125–127.

Ishikawa-Ankerhold, H.C., Ankerhold, R., and Drummen, G.P.C. (2012). Advanced fluorescence microscopy techniques–FRAP, FLIP, FLAP, FRET and FLIM. Molecules *17*, 4047–4132.

Keates, R. (1980). Effects of glycerol on microtubule polymerization kinetics. Biochem Biophys Res Commun *97*, 1163–1169.

Knapp, B.D., Odermatt, P., Rojas, E.R., Cheng, W., He, X., Huang, K.C., and Chang, F. (2019). Decoupling of rates of protein synthesis from cell expansion leads to supergrowth. Cell Syst *9*, 434–445.e6.

Kosetsu, K., de Keijzer, J., Janson, M.E., and Goshima, G. (2013). MICROTUBULE-ASSOCIATED PROTEIN65 is essential for maintenance of phragmoplast bipolarity and formation of the cell plate in Physcomitrella patens. Plant Cell *25*, 4479–4492.

Kozgunova, E., and Goshima, G. (2019). A versatile microfluidic device for highly inclined thin illumination microscopy in the moss Physcomitrella patens. Sci. Rep. *9*, 15182.

Krüger, L.K., Sanchez, J.L., Paoletti, A., and Tran, P.T. (2019). Kinesin-6 regulates cell-size-dependent spindle elongation velocity to keep mitosis duration constant in fission yeast. Elife *8*, e42182.

Kuimova, M.K., Yahioglu, G., Levitt, J.A., and Suhling, K. (2008). Molecular rotor measures viscosity of live cells via fluorescence lifetime imaging. J. Am. Chem. Soc. *130*, 6672–6673.

Lemière, J., and Berro, J. (2018). Adaptation of actin dynamics and membrane tension control for yeast endocytosis. bioRxiv. https://doi.org/10.1101/342030.

Lemière, J., Real-Calderon, P., Holt, L.J., Fai, T.G., and Chang, F. (2021). Control of nuclear size by osmotic forces in *Schizosaccharomyces pombe*. bioRxiv. https://doi.org/10.1101/2021.12.05.471221.

Loiodice, I., Janson, M.E., Tavormina, P., Schaub, S., Bhatt, D., Cochran, R., Czupryna, J., Fu, C., and Tran, P.T. (2019). Quantifying tubulin concentration and microtubule number throughout the fission yeast cell cycle. Biomolecules *9*, 86.

Luby-Phelps, K., Taylor, D.L., and Lanni, F. (1986). Probing the structure of cytoplasm. J. Cell Biol. *102*, 2015–2022.

Machado, S., Mercier, V., and Chiaruttini, N. (2019). LimeSeg: A coarse-grained lipid membrane simulation for 3D image segmentation. BMC Bioinformatics *20*, 2.

Mahamdeh, M., and Howard, J. (2019). Implementation of interference reflection microscopy for label-free, high-speed imaging of microtubules. J. Vis. Exp. *150*. https://doi.org/10.3791/59520.

Marquis, R.E. (1973). Immersion refractometry of isolated bacterial cell walls. J. Bacteriol. *116*, 1273–1279.

Maundrell, K. (1990). nmt1 of fission yeast. A highly transcribed gene completely repressed by thiamine. J. Biol. Chem. *265*, 10857–10864.

Maurer, S.P., Beiling, P., Cope, J., Hoenger, A., and Surrey, T. (2011). GTPγS microtubules mimic the growing microtubule end structure recognized by end-binding proteins (EBs). Proc. Natl. Acad. Sci. *108*, 3988–3993.

Maurer, S.P., Fourniol, F., Bohner, G., Moores, C.A., and Surrey, T. (2012). EBs recognize a nucleotide-dependent structural cap at growing microtubule ends. Cell *149*, 371–382.

Mcguffee, S.R., and Elcock, A.H. (2010). Diffusion, crowding & protein stability in a dynamic molecular model of the bacterial cytoplasm. PLoS Comput. Biol. *6*, e1000694.

Miermont, A., Waharte, F., Hu, S., McClean, M.N., Bottani, S., Léon, S., and Hersen, P. (2013). Severe osmotic compression triggers a slowdown of intracellular signaling, which can be explained by molecular crowding. Proc. Natl. Acad. Sci. USA *110*, 5725–5730.

Milo, R., and Phillips, R. (2015). Cell Biology by the Numbers, 1st ed. (CRC Press).

Minton, A.P. (2006). How can biochemical reactions within cells differ from those in test tubes? J. Cell Sci. *119*, 2863–2869.

Mitchison, T.J. (2019). Colloid osmotic parameterization and measurement of subcellular crowding. Mol. Biol. Cell *30*, 173–180.

Moeendarbary, E., Valon, L., Fritzsche, M., Harris, A.R., Moulding, D.A., Thrasher, A.J., Stride, E., Mahadevan, L., and Charras, G.T. (2013). The cytoplasm of living cells behaves as a poroelastic material. Nat. Mater. *12*, 253–261.

Moreno, S., Klar, A., and Nurse, P. (1991). Molecular genetic analysis of fission yeast Schizosaccharomyces pombe. Methods Enzymol *194*, 795–823.

Munishkina, L.A., Cooper, E.M., Uversky, V.N., and Fink, A.L. (2004). The effect of macromolecular crowding on protein aggregation and amyloid fibril formation. J. Mol. Recognit. *17*, 456–464.

Mutavchiev, D.R., Leda, M., and Sawin, K.E. (2016). Remodeling of the fission yeast Cdc42 cell-polarity module via the Sty1 p38 stress-activated protein kinase pathway. Curr. Biol. *26*, 2921–2928.

Neurohr, G.E., and Amon, A. (2020). Relevance and regulation of cell density. Trends Cell Biol *30*, 213–225.

Obodovskiy, I. (2019). Chapter 34-Basics of biology. Radiation: Fundamentals, Applications, Risks, and Safety (Elsevier), pp. 429–445.

Odde, David J. (1997). Estimation of the diffusion-limited rate of microtubule assembly. Biophysical Journal *73* (1), 88–96.

Odermatt, P.D., Miettinen, T.P., Lemière, J., Kang, J.H., Bostan, E., Manalis, S.R., Huang, K.C., and Chang, F. (2021). Variations of intracellular density during the cell cycle arise from tip-growth regulation in fission yeast. Elife *10*, e64901.

Pérez, P., and Cansado, J. (2010). Cell integrity signaling and response to stress in fission yeast. Curr. Protein Pept. Sci. *11*, 680–692.

Persson, L.B., Ambati, V.S., and Brandman, O. (2020). Cellular control of viscosity counters changes in temperature and energy availability. Cell *183*, 1572–1585.e16.

Pradeep, L., and Udgaonkar, J.B. (2007). Diffusional barrier in the unfolding of a small protein. J. Mol. Biol. *366*, 1016–1028.

Rice, S.A., and Kenney-Wallace, G.A. (1980). Time-resolved fluorescence depolarization studies of rotational relaxation in viscous media. Chem. Phys. *47*, 161–170.

Robertson, A.M., and Hagan, I.M. (2008). Stress-regulated kinase pathways in the recovery tip growth and microtubule dynamics following osmotic stress in *S. pombe*. J. Cell Sci. *121*, 4055–4068.

Salmon, E.D., Saxton, W.M., Leslie, R.J., Karow, M.L., and McIntosh, J.R. (1984). Diffusion coefficient of fluorescein-labeled tubulin in the cytoplasm of embryonic cells of a sea urchin: video image analysis of fluorescence redistribution after photobleaching. J. Cell Biol. *99*, 2157–2164.

Sato, M., Toya, M., and Toda, T. (2009). Visualization of fluorescence-tagged proteins in fission yeast: the analysis of mitotic spindle dynamics using GFP-tubulin under the native promoter. Methods Mol. Biol. *545*, 185–203.

Sawin, K.E., and Tran, P.T. (2006). Cytoplasmic microtubule organization in fission yeast. Yeast *23*, 1001–1014.

Sbalzarini, I.F., and Koumoutsakos, P. (2005). Feature point tracking and trajectory analysis for video imaging in cell biology. J. Struct. Biol. *151* (2), 182–195.

Schindelin, J., Arganda-Carreras, I., Frise, E., Kaynig, V., Longair, M., Pietzsch, T., Preibisch, S., Rueden, C., Saalfeld, S., Schmid, B., et al. (2012). Fiji: an open-source platform for biological-image analysis. Nat. Methods *9*, 676–682.

Schneider, C.A., Rasband, W.S., and Eliceiri, K.W. (2012). NIH Image to ImageJ: 25 years of image analysis. Nat. Methods *9*, 671–675.

Shahid, S., Hassan, M.I., Islam, A., and Ahmad, F. (2017). Size-dependent studies of macromolecular crowding on the thermodynamic stability, structure

and functional activity of proteins: *in vitro* and *in silico* approaches. Biochim. Biophys. Acta Gen. Subj. *1861*, 178–197.

Siegel, J., Suhling, K., Lévêque-Fort, S., Webb, S.E.D., Davis, D.M., Phillips, D., Sabharwal, Y., and French, P.M.W. (2003). Wide-field time-resolved fluorescence anisotropy imaging (TR-FAIM): imaging the rotational mobility of a fluorophore. Rev. Sci. Instrum. *74*, 182–192.

Sozański, K., Ruhnow, F., Wiśniewska, A., Tabaka, M., Diez, S., and Hołyst, R. (2015). Small crowders slow down kinesin-1 stepping by hindering motor domain diffusion. Phys. Rev. Lett. *115*, 218102.

Steinmark, I.E., Chung, P.H., Ziolek, R.M., Cornell, B., Smith, P., Levitt, J.A., Tregidgo, C., Molteni, C., Yahioglu, G., Lorenz, C.D., and Suhling, K. (2020). Time-resolved fluorescence anisotropy of a molecular rotor resolves microscopic viscosity parameters in complex environments. Small *16*, e1907139. https://doi.org/10.1002/smll.201907139.

Suhling, K., Levitt, J., and Chung, P.H. (2014). Time-resolved fluorescence anisotropy imaging. Methods Mol. Biol. *1076*, 503–519.

Suhling, K., Siegel, J., Lanigan, P.M.P., Lévêque-Fort, S., Webb, S.E.D., Phillips, D., Davis, D.M., and French, P.M.W. (2004). Time-resolved fluorescence anisotropy imaging applied to live cells. Opt. Lett. *29*, 584–586.

Tatebe, H., Shimada, K., Uzawa, S., Morigasaki, S., and Shiozaki, K. (2005). Wsh3/Tea4 is a novel cell-end factor essential for bipolar distribution of tea1 and protects cell polarity under environmental stress in *S. pombe*. Curr. Biol. *15*, 1006–1015.

Tran, P.T., Marsh, L., Doye, V., Inoué, S., and Chang, F. (2001). A mechanism for nuclear positioning in fission yeast based on microtubule pushing. J. Cell Biol. *153*, 397–411.

Unsworth, A., Masuda, H., Dhut, S., and Toda, T. (2008). Fission yeast Kinesin-8 Klp5 and Klp6 are interdependent for mitotic nuclear retention and required for proper microtubule dynamics. Mol. Biol. Cell *19*, 5104–5115.

Verkman, A.S., Armijo, M., and Fushimi, K. (1991). Construction and evaluation of a frequency-domain epifluorescence microscope for lifetime and anisotropy decay measurements in subcellular domains. Biophys. Chem. *40*, 117–125.

Walker, R.A., O'Brien, E.T., Pryer, N.K., Soboeiro, M.F., Voter, W.A., Erickson, H.P., and Salmon, E.D. (1988). Dynamic instability of individual microtubules analyzed by video light microscopy: rate constants and transition frequencies. J. Cell Biol. *107*, 1437–1448.

Wang, Z., Shah, J.V., Chen, Z., Sun, C.H., and Berns, M.W. (2004). Fluorescence correlation spectroscopy investigation of a GFP mutant-enhanced cyan fluorescent protein and its tubulin fusion in living cells with two-photon excitation. J. Biomed. Opt. *9*, 395–403.

Watari, J., Kobae, Y., Yamaki, S., Yamada, K., Toyofuku, K., Tabuchi, T., and Shiratake, K. (2004). Identification of sorbitol transporters expressed in the phloem of apple source leaves. Plant Cell Physiol *45*, 1032–1041.

Wieczorek, M., Chaaban, S., and Brouhard, G.J. (2013). Macromolecular crowding pushes catalyzed microtubule growth to near the theoretical limit. Cel. Mol. Bioeng. *6*, 383–392.

Wlodarski, M., Mancini, L., Raciti, B., Sclavi, B., Lagomarsino, M.C., and Cicuta, P. (2020). Cytosolic crowding drives the dynamics of both genome and cytosol in *Escherichia coli* challenged with sub-lethal antibiotic treatments. iScience *23*, 101560.

Wood, R.E., Wirth, F.P., and Morgan, H.E. (1968). Glucose permeability of lipid bilayer membranes. Biochim. Biophys. Acta *163*, 171–178.

Xiang, Y., Surovtsev, I., Chang, Y., Govers, S., Parry, B., Liu, J., and Jacobs-Wagner, C. (2020). Solvent quality and chromosome folding in *Escherichia coli*. bioRxiv. https://doi.org/10.1101/2020.07.09.195560.

Yamada, M., Miki, T., and Goshima, G. (2016). Imaging mitosis in the moss *Physcomitrella patens*. Methods Mol. Biol. *1413*, 263–282.

Yu, I., Mori, T., Ando, T., Harada, R., Jung, J., Sugita, Y., and Feig, M. (2016). Biomolecular interactions modulate macromolecular structure and dynamics in atomistic model of a bacterial cytoplasm. Elife *5*, 1–22.

STAR★METHODS

KEY RESOURCE TABLE

Reagent or resource	Source	Identifier
Experimental models: *Schizosaccharomyces pombe* strains		
h⁻ wt (972)	Chang lab collection	FC15
h⁺ GFP-atb2:kanMX ade6- leu1-32 ura4-D18	Chang lab collection	FC2861
h⁺ sty1::ura4+ GFP-atb2:kanMX	this manuscript	AM23 / FC3283
h⁻ mal3::natMX leu1-32::SV40-GFP-atb2[LEU1+] ade6- leu1- ura4-	Chang lab collection	FC2343
h⁺ alp14::natMX leu1-32::SV40-GFP-atb2[LEU1+] leu1- ura4-	Chang lab collection	FC2357
h⁻rps802-GFP::kan^R leu1-32 ura4-D18 ade6-216	Knapp et al., 2019	FC3208
alp14-GFP-kan atb2-mCh::hph	this manuscript	AM53 / FC3284
mal3-GFP:kanMX atb2-mCh::hph	this manuscript	AM57 / FC3285
pREP41X_AqLs:Sapphire	this manuscript	AM35 / FC3286
pREP41X_PfV:Sapphire	this manuscript	AM38 / FC3287
h⁻ ade6<<mCherry-psy1 ish1-GFP:kanMX gpd1::hphMX6 ura4-D18 ade6	this manuscript	JL160 / FC3290
h⁻ pREp41X-Pfv-Sapphire ade6-M216 leu1-32 ura4-D18 his3-D1	this manuscript	JL110 / FC3289
tip1::kanMX leu1-32::pSV40-GFP-atb2(leu1+)	this manuscript	AM94 / FC3325
klp5::ura+ GFP-atb2:kanMX	this manuscript	AM92 / FC3326
h⁺ hta1-mCherry:kanMX GFP-atb2:kanMX ade6- leu1-32 ura4- his+	this manuscript	AM2 / FC2859
Experimental model: *Physcomitrella patens* line		
EB1-Citrine mCherry-tubulin	Kosetsu et al., 2013	GPH0379#2
Chemicals		
YES 225	Sunrise Science Products	2011-500
Edinburgh Minimal Media (EMM)	MP Biomedicals	4110-032
Agar	Difco	281210
D-sorbitol	Sigma	S1876
Adenine	Sigma	A9126
Leucine	Sigma	L8000
Histidine	Sigma	H8000
Uracil	Sigma	U0750
Carbendazim	Sigma	378674-100G
Lectin	Sigma	L1395
Fluorescein Diacetate	Sigma	F7378
Lallzyme MMX	Scott laboratories	016207
Bovine Serum Albumin	Fisher Scientific	9048-46-8
Paraformaldehyde	Thermo Fisher	28906
Software		
FIJI	Schindelin et al., 2012	https://imagej.net/contribute/fiji
ImageJ	Schneider et al., 2012	https://imagej.nih.gov/ij/
MOSAIC for imageJ	Sbalzarini and Koumoutsakos, 2005	https://imagej.net/plugins/mosaicsuite
LimeSeg	Machado et al., 2019	https://imagej.net/plugins/limeseg
Matlab	Mathworks®	https://www.mathworks.com/
Micromanager	Edelstein et al., 2014	https://micro-manager.org/Citing_Micro-Manager

RESOURCE AVAILABILITY

Lead contact

Further information and requests for resources and reagents should be directed to and will be fulfilled by the lead contact, Fred Chang (fred.chang@ucsf.edu).

Materials availability

Yeast strains generated in this study are available upon request.

Data and code availability

Data generated in this study are available upon request.

EXPERIMENTAL MODEL AND SUBJECT DETAILS

Fission yeast

Standard methods for growing and genetically manipulating *Schizosaccharomyces pombe* were used (Moreno et al., 1991). For most experiments, cells were grown overnight in Yeast Extract (YE5S) medium (here called YE) with shaking at 30 °C to exponential phase (OD_{600} between 0.2 - 0.8). See Key resource table. for reagents and strains details.

Physcomitrium (Physcomitrella) patens

Moss cells were grown as described previously (Yamada et al., 2016). Caulonemal cells were mounted in microfluidic devices at room temperature as described previously (Kozgunova and Goshima, 2019).

Mammalian cells

PTK2 cells stably expressing GFP-tubulin were grown in DMEM/F12 medium supplemented with 10% fetal bovine serum (FBS) and 1% antibiotic-antimycotic (Thermofisher #15240062) (10% DMEM/F12) with 5% CO2. The day before experiments, cells were plated in 35 mm glass bottom dish (Ibidi #81218), incubated in 2 ml of medium and left overnight at 37 °C and 5% CO2 to allow them to spread properly.

METHOD DETAILS

Yeast strain construction

Cassettes for expressing GEMs (20 nm, AqLs-Sapphire; 40 nm, PfV-Sapphire), were cloned into the fission yeast pREP41X expression vector from pRS306 budding yeast expression vectors (Delarue et al., 2018). Briefly, GEMs expression cassettes were amplified via PCR and inserted into pREP41X via Gibson assembly at the XhoI site. The primers used for PCR are described in the supplementary table.

Protoplast preparation

S. pombe cells were grown in YE5S liquid culture at 30 °C to exponential phase, harvested, and washed with SCS buffer (20 mM citrate buffer, 1 M D-sorbitol, pH 5.8), then resuspended in SCS buffer supplemented with 0.1 g/mL Lallzyme (Lallemand, Montreal, Canada) (Flor-Parra et al., 2014). Cells were digested for 10 min at 37 °C with gentle shaking in the dark. The resulting protoplasts were gently washed twice in YE5S medium with 0.2-1 M D-sorbitol, using gentle centrifugation (2 min at 0.4 rcf).

Imaging of fission yeast

S. pombe cells and protoplasts were imaged in commercial microchannels (Ibidi μ-slide VI 0.4 slides; Ibidi 80606, Ibiditreat #1.5). Channels were pre-treated with 50 μl of 100 μg/ml lectin solution for 5 min at room temperature. The lectin solution was removed by pipetting and 50 μl of cell culture were introduced. After incubation for 3 to 10 minutes to allow cells to adhere to the lectin, the cells were washed with YE5S. For hyper-osmotic shocks, the medium was manually removed from the channel via pipetting and quickly replaced with hyper-osmotic media as indicated.

Microtubule dynamics

Yeast cells expressing GFP-tubulin (see Key Resources Table) were observed with a 488 nm excitation laser at 100 ms of exposure per z-slice (1 μm spacing, 7 slices) at 0.1 Hz, with a 60x objective (CFI Plan Apochromat VC 60XC WI) on a Nikon TI-E equipped with a spinning-disk confocal head (CSU10, Yokogawa) and an EM-CCD camera (Hammamatsu C9100-13). MTs in protoplasts were imaged with similar settings but the number of z-slices was changed according to protoplasts diameter.

Spindle elongation

Yeast cells expressing GFP-tubulin and mCh-histones were observed with 488 nm and 561 nm excitation lasers at 100 ms of exposure per z-slice per channel (1 μm spacing, 7 slices) at 0.017 Hz, with a 60x objective (CFI Plan Apochromat VC 60XC WI) on a Nikon TI-E equipped with a spinning-disk confocal head (CSU10, Yokogawa) and an EM-CCD camera (Hammamatsu C9100-13).

Intracellular density

Intracellular density was measured using a refractive index mismatch approach (Bateman et al., 1966; Marquis, 1973; Odermatt et al., 2021; Wlodarski et al., 2020). Cells from 1 ml of exponentially growing culture were pelleted by centrifugation (10 000 g, 2 minutes) then resuspended in 1 mL of YE or YE + 1.5 M sorbitol containing various amount of BSA. Immediately after resuspension, the sample was split in two cuvettes and OD 600 was measured. Blanked were measured before on YE or YE + 1.5M sorbitol. In YE + 1.5 M sorbitol, we could not produce solutions containing more than 150 mg of BSA per milliliter due to solubility concerns. The OD readout was normalized to YE or YE + 1.5 M sorbitol without BSA. The projection of the linear fits onto the x-axis gives an estimate of the intracellular density for each condition.

Protoplast volume

Protoplasts were resuspended in YE5S medium with 0.2-1 M D-sorbitol, then imaged with a 561 nm excitation laser (mCherry-Psy1) at 100 ms of exposure per z-slice (0.5 μm spacing), with the 60x objective, microscope, and camera used for MT dynamics.

GEMs diffusion

Yeast cells were imaged with a 60x TIRF objective (Nikon, MRD01691) on a Nikon TI-E equipped with a Nikon TIRF system and a SCMOS camera (Andor, Ixon Ultra 888). Protoplasts were imaged on a Nikon TI-2 equipped with a Diskovery Multi-modal imaging system from Andor and a SCMOS camera (Andor, Ixon Ultra 888) using a 60x TIRF objective (Nikon, MRD01691). Cells were imaged at 100 Hz, in TIRF, for 10 s with a 488 nm excitation laser.

Tubulin diffusion

Cells were imaged at 0.2 Hz, with a 60x TIRF objective (Nikon, MRD01691) on a Nikon TI-2 equipped with a Diskovery Multi-modal imaging system from Andor and a SCMOS camera (Andor, Ixon Ultra 888). Cells were imaged using spinning disk with pinhole of 100 μm. Cells were imaged at 488 nm laser excitation; the bleaching laser was a 473 nm laser controlled by a UGA-42 Firefly (Rapp OptoElectronic).

FDA labeling

Cells were labeled with 100 μM fluorescein diacetate (Sigma, F7378) for 30 min at room temp with agitation. Yeast cells expressing GFP-tubulin (see Key Resources Table) were observed with a 488 nm excitation laser at 100 ms, with a 60x objective (CFI Plan Apochromat VC 60XC WI) on a Nikon TI-E equipped with a spinning-disk confocal head (CSU10, Yokogawa) and an EM-CCD camera (Hammamatsu C9100-13).

Osmotic shock experiments

Hyperosmotic shifts

Cells were grown in rich YE5S medium, mounted into microchannels, and then treated with YE5S containing various concentrations of sorbitol while on the microscope stage at room temperature. Loss of water after the switch of medium is almost instantaneous (<30 s). To minimize adaptation responses (Tatebe et al., 2005), imaging was initiated as soon as possible (<1 min) after adding sorbitol.

Osmotic oscillations

Cells were introduced into a microfluidic system (Cell Asics) as described in (Knapp et al., 2019) then the media in the chamber was oscillated; YE for 5 minutes then YE with 1.5 M sorbitol for 3 or 5 minutes. During the oscillations cells were imaged for MT dynamic measurement as described above.

Cold treatment

Yeast cells expressing GFP-tubulin were pelleted gently and resuspended in YE containing 0, 0.5, 1, or 1.5 M sorbitol. Each culture was split into two tubes; one was incubated for 5 min at room temperature and the other was incubated on ice for 5 min. Cells were fixed by adding 16% paraformaldehyde to the medium for a final concentration of 4%. Cell were then imaged in lectin-treated Ibidi chambers.

Osmotic shifts of protoplasts

After cell-wall digestion, protoplasts were gently washed twice in YE5S with 0.4 M D-sorbitol using gentle centrifugation (2 min at 0.4 rcf), then placed in the Ibidi chamber for imaging. Medium was exchanged manually with hypo- or hyper-tonic medium right before imaging. YE + 0.4 M sorbitol was close to isotonic conditions, as determined by comparing volumes and GEMs dynamics to yeast cells. Thus, protoplasts resuspended in YE + 0.2, 0.25, or 0.3 M sorbitol were in hypo-tonic conditions, while protoplasts in YE + 0.5 or 1 M sorbitol were in hyper-tonic conditions.

Measurements of MT dynamic parameters and cell volume in yeast and protoplasts

MT dynamics

Measurements of MT dynamic parameters were obtained using analyses of kymographs of GFP-tubulin expressing cells. Images of individual cells were cropped and multiple MT bundles per cell were selected from maximum intensity projection of the z-stack. Kymographs were made and analyzed with the KymoToolBox plugin of ImageJ (Schneider et al., 2012).

Volume

The effects of sorbitol on cell volume were determined from the change in cell width measured from brightfield images at the cell midplane. This calculation was established previously and is based on the isotropic mechanics of the cell-wall and the rod shape of the cell (Atilgan et al., 2015). Protoplast volume was measured in 3D from Z-stack fluorescence images of cells expressing markers for the plasma membrane (mCherry-Psy1) using LimeSeg, a Fiji pulg-in (Machado et al., 2019; Schindelin et al., 2012).

Spindle elongation

Spindle length was manually measured on maximum intensity projections using the tubulin signal. Spindles were of various length at the beginning of the experiment so only spindle shorter than 2.5 μm at the starts of the experiments were analyzed. Spindle length was normalized to the first time point for each spindle. Instantaneous elongation rate was measured for each spindle and then averaged.

Mal3 and Alp14 localization

Fluorescence intensity of Mal3-GFP and Alp14-GFP were measured on sum z-projection. The average intensity along the last 0.5 μm of the MTs was measured averaging over 3 pixels wide. The intensity of the GFP signal was normalized to the intensity of the tubulin-mCherry. Datasets were compared using Mann-Whitney u-test, for Alp14 the difference is non-significant with p-value = 0.11 and for Mal3 the difference is significant with p-value < 0.001.

FLIP experiments

Cells expressing GFP-tubulin were mounted in microchannels and treated with 25 μg/ml methyl benzimidazol-2-yl-carbamate (MBC) for >1 min to depolymerize MTs. Cells were then subjected to repeated photobleaching with a focused 473 nm laser in a 1-μm region near the cell tip using a UGA-42 Firefly system from RapOpto. Cells of similar size (∼ 12 μm long) were photobleached in order to reduce variability in the resulting data. Fluorescence decrease was followed in the half of the cell submitted to the bleaching sequence to avoid the effects of diffusion around/through the nucleus. Fluorescence decrease curves were normalized and aligned to the time point preceding the activation of the bleach sequence.

A calibrated 1D Brownian model of diffusion was used to simulate the fluorescence decrease in a 6 μm tube (half of a cell 12 μm in length). Bleaching rate, region size, and position were matched to the experimental setup. Particles positions were updated every 0.01 s. The decrease in the number of unbleached particles in the model was read out every 5 s (matching the imaging frequency) and normalized to the total number of particles. The insensitivity of the model to the total number of particles and to the time interval used was established by changing these parameters across three orders of magnitude, without significant effect on the outputs. Plots of fluorescence decrease for various diffusion rates in the model were compared to the experimentally measured values to obtain the estimated tubulin diffusion rates.

Microrheology with GEMs nanoparticles

GEM fusion proteins were expressed from pREP41X-based expression vectors from the thiamine-regulated nmt1* promoter (Maundrell, 1990). Transformants containing these plasmids were maintained on EMM-leu medium. The day before imaging, cells were inoculated in EMM-leu medium containing 0.05 μg/mL thiamine to allow a low level of construct expression. These conditions generally produced a few tens of GEM nanoparticles per cell. Overexpression of the GEMs commonly produced cells with single, bright, non-motile aggregates. Cells expressing GEMs were selected for sparse numbers of labeled motile nanoparticles and imaged at 100 Hz intervals. Individual cells were cropped for analysis. Nanoparticles in each cell were tracked using the MOSAIC plugin (Fiji ImageJ), and the effective diffusion rate was determined from mean squared displacement (MSD) plots as previously (Delarue et al., 2018). Briefly, tracks shorter than 10 timepoints were excluded from the MSD analysis. The following fit was used on the first 100 ms to extract the diffusion value for trajectories longer than 10 timepoints: MSD = 4Dt. The following parameters were used for the 2D Brownian dynamics tracking in MOSAIC: radius = 3, cutoff = 0, per/abs = 0.2-0.3, link = 1, and displacement = 6.

MT dynamics in moss cells

Osmotic shocks

For osmotic shock, observation medium was removed manually via aspiration with a syringe, and medium with sorbitol was subsequently introduced with a syringe.

Microtubule dynamics

Cells were imaged on a Nikon TI-E TIRF system with a 60x TIRF objective (Nikon, MRD01691) and a SCMOS camera (Andor, Ixon Ultra 888). MT dynamic parameters were obtained using kymographs. Kymographs were made and analyzed with the KymoToolBox plugin of ImageJ.

Analysis

Measurements of MT dynamic parameters were obtained using kymographs of PTK2 cells stably expressing GFP-tubulin. Region of interest (ROIs) of individual cells were cropped and multiple MTs per ROI were selected. Kymographs were made and analyzed with the KymographBuilder plugin of ImageJ.

MT dynamics in mammalian cells

Osmotic shocks

The media contained in the 35 mm glass bottom dish was manually replaced by 2 ml of 10% DMEM/F12 prewarmed to 37 °C containing various concentrations of sorbitol while on the microscope stage controlled with the Chamlide TC incubator (kept at 37 °C and 5% CO2). Loss of water after the switch of medium is almost instantaneous (<30 s). To minimize adaptation responses, imaging was initiated 3 minutes before the switch of medium and continued for 4 minutes after adding sorbitol.

Microtubule dynamics

PTK2 cells stably expressing GFP-tubulin plated in 35 mm glass bottom dish were observed with a 488 nm excitation laser at 200 ms of exposure at 0.2 Hz with a 60x objective (Plan Apo VC 60x/1.40 oil) in a Nikon TI-E equipped with a spinning disk confocal head (CSU-X1, Yokogawa) and a CCD camera (QImaging Retiga R3). The cell culture conditions on the microscope stage were controlled with the Chamlide TC incubator (kept at 37 °C and 5% CO2).

Analysis

Measurements of MT dynamic parameters were obtained using kymographs of PTK2 cells stably expressing GFP-tubulin. Region of interest (ROIs) of individual cells were cropped and multiple MTs per ROI were selected. Kymographs were made and analyzed with the KymographBuilder plugin of ImageJ.

MT dynamics *in vitro*

Tubulin preparation

Tubulin was purified from juvenile bovine brains via cycles of polymerization and depolymerization, as described previously (Ashford and Hyman, 2006). GMPCPP-stabilized MT seeds were prepared by polymerizing a 1:4 molar ratio of tetramethylrhodamine (TAMRA, ThermoFisher Scientific) labeled:unlabeled tubulin (Hyman, 1991) in the presence of GMPCPP (Jena Biosciences) in two cycles, as described previously (Gell et al., 2011).

MT reconstitution assay

Dynamic MTs were imaged in a reconstitution assay from surface-bound, stabilized MT seeds (Gell et al., 2011). Cover glass was cleaned, as previously described (Helenius et al., 2006). Two silanized cover glasses (22 x 22 mm and 18 x 18 mm) were separated by multiple strips of double-sided tape on custom-machined mounts to create channels for solution exchange. Channels were prepared for experiments by flowing in anti-TAMRA antibodies (ThermoFisher Scientific) and blocking with 1% Pluronic F-127 for 20 min. Channels were rinsed three times with BRB80 before flowing in seeds and placing the chamber on the microscope stage, where the objective was heated to 32 °C with a CU-501 Chamlide lens warmer (Live Cell Instrument).

Dynamic MTs were grown from GMPCPP seeds by filling the channel with 10 μM tubulin in reaction buffer: BRB80 (80 mM PIPES-KOH [pH 6.9], 1 mM EGTA, 1 mM $MgCl_2$) plus 1 mM GTP, 0.1 mg/mL bovine serum albumin, 10 mM dithiothreitol, 250 nM glucose oxidase, 64 nM catalase, and 40 mM D-glucose. Reaction buffer was prepared on ice before being flowed into the channel with a piece of filter paper. A 60% (v/v) glycerol stock solution in BRB80 was added to the indicated final concentrations. For consistency, a large aliquot of tubulin was thawed on the day of each experiment, sub-aliquoted, and stored in liquid nitrogen. A separate sub-aliquot was thawed for each individual experiment. Glycerol concentrations from 0-15% (v/v) were tested. We note that the effects of glycerol concentrations $\geq$20% were not measurable as no depolymerization events were observed because of the high levels of spontaneous nucleation and inhibition of catastrophes at those glycerol concentrations.

For the buffer exchange, microtubules were grown from 10 μM tubulin in BRB80 buffer with 10% glycerol at 32 °C for at a few minutes. Then, the buffer was manually exchange using a pipette and a piece of filter paper. The buffer exchange happened quickly < 1 minute. The final buffer contained 0 μM tubulin and various amount of glycerol.

Interference reflection microscopy

Dynamic label-free MTs were imaged with interference reflection microscopy (IRM) as described previously (Mahamdeh and Howard, 2019).

MT dynamics

MT dynamics was analyzed using kymographs as described above.

Viscosity measurements in vitro

Viscosities of glycerol solutions were measured using an mVROC Viscometer (Rheosense) at room temperature (23°C as measured by the viscometer). Measurements were made at a flow rate of 1000 μl/min for 5 sec for three replicates of each solution. Using the expected values of viscosity for similar water-glycerol mixtures (http://www.met.reading.ac.uk/~sws04cdw/viscosity_calc.html) at 23°C and 32°C, we extrapolated the viscosity of the buffers at 32°C from the measurements at 23°C.

Cytoplasmic viscosity measurements

FDA labeling

Wild-type fission yeast cells were grown in YE overnight at room temperature with agitation to below saturation. Cells were labeled with 100 μM fluorescein diacetate (Sigma, F7378) for 30 min at room temperature with agitation.

Time-resolved fluorescence anisotropy

Cells were imaged in a Ibidi μ-slide VI 0.4 (Ibidi 80606, Ibiditreat #1.5) treated with lectin on an inverted TCS-SP2 microscope (Leica Microsystems, Germany) while the time- and polarization-resolved intensity decay was measured on SPC-150 TCSPC boards (Becker & Hickl, Germany). The emission was split using a polarizing beam splitter. Fluorescein diacetate (FDA) was excited using a picosecond-pulsed (90 ps optical pulse width, 20 MHz repetition rate) 467 nm diode laser (Hamamatsu, Japan) through a 63X 1.2 NA water objective, with a 485 nm dichroic mirror and a 500 nm long pass filter. All measurements were performed at room temperature (22°C).

Parallel ($I_{\parallel}$) and perpendicular ($I_{\perp}$) intensity decays were used to calculate the anisotropy decay, according to

$$r(t) = \left(I(t)_{\parallel} - G * I(t)_{\perp}\right) / \left(I(t)_{\parallel} + z * G * I(t)_{\perp}\right)$$

where z = 1 to account for the depolarization of the high NA objective and G was 0.96. Z was determined by comparing the calculated total intensity decay

$$I_{tot} = I_{\parallel} + z * GI_{\perp}$$

of fluorescein measured on the 63x objective and measured on a 5x objective, altering the value of z between 2 and 1 until the lifetime was an exact match (Suhling et al., 2014). G is a correction factor to account for the sensitivity of the two detectors and is calculated by taking the tail value of

$$G = I(t)_{\parallel}/I(t)_{\perp}$$

after tail-matching of the parallel and perpendicular decays by adjustment of the polarizing beam splitter.

Parallel and perpendicular intensity decays were summed over six measurements (3 measurements x 2 biological repeats) to obtain high photon counts, after ensuring negligible variation between measurements and repeats. The resulting time-resolved anisotropy decay was fit to a monoexponentially decaying model according to

$$y = A * exp^{\left(-\frac{t}{\theta}\right)} + y_0$$

where θ is the rotational correlation time, A is the amplitude of the decay (in terms of the anisotropy decay, this value is equal to r_0-r_∞), and y_0 is the level to which the anisotropy decays (properly known as r_∞). The rotational correlation time was converted into a viscosity value in cP using a calibration plot in the relevant viscosity region.

Fluorescein calibration curve

Methanol solutions containing various amounts of glycerol (0-40%) were prepared. Solution viscosities at room temperature (22 °C) were established previously using a rheometric expansion system rheometer (ARES) (Kuimova et al., 2008; Steinmark et al., 2020). Fluorescein (10 μM) was added to the solutions and fluorescence was measured at room temperature to extract the rotational correlation times as described above. Note that the calibration was carried out on a 5x air objective; thus, z was taken as 2. Data from the literature (Clayton et al., 2002; Rice and Kenney-Wallace, 1980; Suhling et al., 2004; Verkman et al., 1991) were include in the calibration.

Anisotropy decay

Anisotropy data were fitted using GraphPad Prism. Fits used $1/STD^2$ weighting and were limited to the first 10 ns of recording. Best-fit values for each parameter and condition were obtained with a F-test. Best fits were different with p-value = 0.0003.

Normalizations

MT dynamics versus cellular volume

MT dynamics and cell volume in yeast were normalized to the YE condition (no sorbitol). In protoplasts MT dynamics and volume were normalized to the 0.4 M sorbitol condition.

GEMs diffusion versus volume

Diffusion values and volumes were normalized to the YE (no sorbitol condition) for yeast and to the 0.4 M sorbitol condition for protoplasts.

Polymerization rate versus depolymerization rate

For yeast, data rates were normalized to the YE (no sorbitol) condition. For protoplasts, data were normalized to the 0.4 M sorbitol condition. For moss, data were normalized to the BCD (no sorbitol) condition. For *in vitro*, data were normalized to the BRB 80 (no glycerol) condition. For the model, data were normalized to the k_+= 1.25 /pf/μM condition. A linear fit on the normalized data from the model gives a slope of 1.1 +/- 0.2. Normalized data from all the other systems (yeast cells, yeast protoplasts, moss cells, in vitro) collapse on the same slope according to a F-test. P values were 0.2, 0.9, 0.8, and 0.38 for yeast cells, yeast protoplasts, moss cells and *in vitro* respectively.